

Special Collection:

Science from the Surface Water and Ocean Topography Satellite Mission

Key Points:

- Vertical velocities can be coherently reconstructed in the Southern Ocean at scales down to 30–40 km
- Vertical heat fluxes can be retrieved using effective surface quasi-geostrophic reconstruction and are dominated by vertical velocities
- Vertical velocities reconstructed from SWOT observations have 50% more variance than those derived from traditional altimetry

Correspondence to:

E. Carli,
elisa.carli@univ-tlse3.fr

Citation:

Carli, E., Siegelman, L., Morrow, R., & Vergara, O. (2024). Surface quasi-geostrophic reconstruction of vertical velocities and vertical heat fluxes in the Southern Ocean: Perspectives for SWOT. *Journal of Geophysical Research: Oceans*, 129, e2024JC021216. <https://doi.org/10.1029/2024JC021216>

Received 14 APR 2024

Accepted 21 AUG 2024




Author Contributions:

Conceptualization: Elisa Carli, Lia Siegelman, Rosemary Morrow
Data curation: Elisa Carli
Formal analysis: Elisa Carli, Lia Siegelman
Investigation: Elisa Carli, Lia Siegelman, Rosemary Morrow
Methodology: Elisa Carli, Lia Siegelman, Rosemary Morrow
Software: Elisa Carli, Lia Siegelman
Supervision: Lia Siegelman, Rosemary Morrow, Oscar Vergara
Validation: Elisa Carli
Visualization: Elisa Carli
Writing – original draft: Elisa Carli

© 2024 The Author(s).

This is an open access article under the terms of the [Creative Commons Attribution-NonCommercial](https://creativecommons.org/licenses/by-nc/4.0/) License, which permits use, distribution and reproduction in any medium, provided the original work is properly cited and is not used for commercial purposes.

Surface Quasi Geostrophic Reconstruction of Vertical Velocities and Vertical Heat Fluxes in the Southern Ocean: Perspectives for SWOT

Elisa Carli¹ , Lia Siegelman² , Rosemary Morrow¹ , and Oscar Vergara^{1,3} 

¹Laboratoire d'Etudes en Géophysique et Oceanographie Spatiale (LEGOS) [CNES, UT3, CNRS, IRD], Toulouse, France,

²Scripps Institution of Oceanography, UC San Diego, La Jolla, CA, USA, ³Collecte Localisation Satellites, Ramonville Saint Agne, France

Abstract Mesoscale currents account for 80% of the ocean's kinetic energy, whereas submesoscale currents capture 50% of the vertical velocity variance. SWOT's first sea surface height (SSH) observations have a spatial resolution an order of magnitude greater than traditional nadir-looking altimeters and capture mesoscale and submesoscale features. This enables the derivation of submesoscale vertical velocities, crucial for the vertical transport of heat, carbon and nutrients between the ocean interior and the surface. This work focuses on a mesoscale energetic region south of Tasmania using a coupled ocean-atmosphere simulation at km-scale resolution and preliminary SWOT SSH observations. Vertical velocities (w), temperature anomalies and vertical heat fluxes (VHF) from the surface down to 1,000 m are reconstructed using effective surface Quasi-Geostrophic (sQG) theory. An independent method for reconstructing temperature anomalies, mimicking an operational gridded product, is also developed. Results show that sQG reconstructs 90% of the modeled w and VHF rms at scales down to 30 km just below the mixed layer and 50%–70% of the rms for scales larger than 70 km at greater depth, with a spatial correlation of ~ 0.6 . The reconstruction is spectrally coherent (>0.65) for scales larger than 30–40 km at the surface, slightly degrading (~ 0.55) at depth. Two temperature anomaly data sets yield similar results, indicating the dominance of w on VHF. The RMS of sQG w and VHF derived from SWOT are twice as large as those derived from conventional altimetry, highlighting the potential of SWOT for reconstructing energetic meso and submesoscale dynamics in the ocean interior.

Plain Language Summary This work focuses on vertical ocean dynamics induced by small-scale ocean surface currents, especially those at the mesoscale and submesoscale (20–100 km in diameter). These ocean vertical velocities pump heat and carbon from the surface to depth and carry nutrients important for biomass development. Our motivation is the first data from the new satellite SWOT (Surface Water and Ocean Topography), which provides observations of surface geostrophic currents at much higher resolution compared to traditional satellites. We study a Southern Ocean area near Tasmania using a realistic coupled ocean-atmosphere simulation at a km-scale resolution and initial SWOT data and reconstruct vertical velocities, temperature, and heat fluxes using a vertical projection theory. Results show that the vertical reconstruction coherently represents ocean vertical velocities and heat fluxes below the surface mixed layer larger than 30–40 km and that smaller scales are not well reconstructed. In the computation of vertical heat fluxes, we compare two different ways of measuring temperature anomalies, finding that, overall, the difference is not significant because vertical velocities dominate the heat fluxes. This study highlights the potential of SWOT for studying small-scale ocean dynamics at the surface and reconstructed at depth.

1. Introduction

Studying oceanic vertical exchanges is paramount because the global ocean is responsible for storing up to 93% of the energy imbalance due to global warming (Rhein et al., 2013), and has absorbed about 30% of total anthropogenic carbon dioxide emissions since the 1980's (Intergovernmental Panel On Climate Change (IPCC), 2022). Observing the dynamical processes that carry this heat and carbon into the ocean interior is still a major challenge in oceanography. The ocean is also highly turbulent. Cyclonic and anticyclonic eddies, ubiquitous and very energetic mesoscale structures, contribute to the energetics of the oceanic circulation, particularly in the western boundary currents and the Antarctic Circumpolar Current (ACC). Mesoscale eddies (50–300 km) impact the lateral stirring and structure of tracers, setting the ocean distribution of heat, salt, carbon, nutrients and biomass

Writing – review & editing: Elisa Carli,
Lia Siegelman, Rosemary Morrow,
Oscar Vergara

(Franks et al., 1986; Mahadevan & Archer, 2000; Martin et al., 2002; Strass, 1992). Their primary role is now recognized also in driving global upward vertical heat transport (Llort et al., 2018; Rintoul, 2018). Griffies et al. (2015) found that the representation of the mesoscale in climate models can largely influence lateral and vertical heat transport. Therefore, it is fundamental to include a rich representation of the ocean mesoscale in model simulations or employ a correct parametrization. However, numerical models do not fully agree on the magnitude of the eddies' impact on the vertical tracer distribution (McGillicuddy et al., 2007) and observations of these 3D dynamical structures are limited. In situ observations of vertical velocities are rare, difficult to measure and have limited coverage in space and time. Satellite infrared and color images show submesoscale horizontal filamentary structures between the eddies, which greatly contribute to the nutrient supply, closing the nutrient budget (Lévy, 2024), but their observations are limited to the ocean surface and in clear sky conditions. Traditional altimetry surface geostrophic velocities have a resolution of around 150 km (Ballarotta et al., 2019) and are thus not able to resolve the small and very energetic scales predominant in the Southern Ocean, where the Rossby radius is small.

The Surface Water and Ocean Topography (SWOT) wide-swath altimeter mission launched in December 2022 (Fu et al., 2024; Morrow et al., 2019) brings a new 2D observation of these scales, being able to observe small ocean structures of 5–10 km with a time coverage in the order of a few days or better at high latitudes. The first SWOT data indicate that the spectral level noise is even lower than the initial science requirement by one order of magnitude at small scales, showing ocean circulation processes at scales down to ~5 km (Fu et al., 2024). After careful editing and processing (Dibarboure et al., 2023), this allows a more precise estimate of ocean sea level elevation, and its derived geostrophic currents, vorticity and strain. These are key properties for reconstructing the 3D ocean circulation from 2D surface satellite observations, which has long been a goal in oceanography.

Different methodologies have been developed to extend surface observations into the ocean interior and estimate vertical velocities as the vector for the vertical transport of heat, carbon, and nutrients. The classical Omega equation (Hoskins et al., 1978) has been widely used to study the balanced motions associated with fronts (Allen et al., 2001; Martin & Richards, 2001; Rudnick, 1996; Tintoré et al., 1991), but the availability of high-resolution data within mesoscale eddies remains a challenge for its application on a larger scale. To explain energy redistribution through different scales, the interior-quasi-geostrophic (QG) and surface-quasi-geostrophic (sQG) theories are often applied. QG is based on a small Rossby number approximation (Charney, 1971; Rhines, 1979). Motions are assumed not to be influenced by vertical boundary conditions and surface density anomalies are assumed to be zero (Klein & Lapeyre, 2009). McWilliams (1989) found that increasing the resolution in three dimensions does not significantly change the QG turbulence. sQG, on the other hand, considers nonzero surface density perturbations, which cascade to small scales leading to small-scale surface frontogenesis (Lapeyre & Klein, 2006). In this case, the potential vorticity (PV) is assumed to be uniform in the interior of the domain. The main limitation of sQG is that when the resolution is high, small-scale structures may have high vorticity values of the order of f (the Coriolis parameter). These structures depart from sQG and are subject to ageostrophic frontogenesis (Klein et al., 2008). Lapeyre and Klein (2006) define an “effective” sQG model based on the same assumptions, which allows the diagnosis of the 3D dynamics in the upper ocean from either the sea surface height (SSH) or surface buoyancy. This present work explores this “effective” sQG solution. The gain in spatial resolution from the new SWOT observations motivates renewed interest in using sQG with altimetry data to infer the 3D dynamical structures in the energetic Southern Ocean region (Qiu et al., 2020; Su et al., 2018; Wang et al., 2013).

The primary objective of this work is to assess the potential of the effective sQG methodology to reconstruct the vertical velocities and vertical heat fluxes within the first 1,000 m of the water column in the energetic Polar Front region of the ACC, downstream of the SouthEast Indian Ridge. The sQG vertical reconstruction is first assessed against the full fields from a realistic ocean model, before being applied to SWOT and conventional altimetry surface data. This region was chosen since it has a strong mesoscale field well adapted to an sQG formalism, and an intensive field campaign was undertaken in November and December 2023, which will provide in situ validation of the vertical reconstruction technique in a following study. The region is dynamically inhomogeneous, with strong water mass variations across the energetic Polar front. Whilst it has relatively flat bottom bathymetry, the energetic dynamics have strong topographic control from ocean ridges upstream and downstream (Figure 1), and we will explore the sQG reconstruction capabilities in this complex dynamical regime. Although similar studies have assessed the sQG reconstruction of vertical velocities in other regions, the primary focus of this study is the reconstruction of both vertical velocities and vertical heat fluxes, the real novelty of our work. Once we have

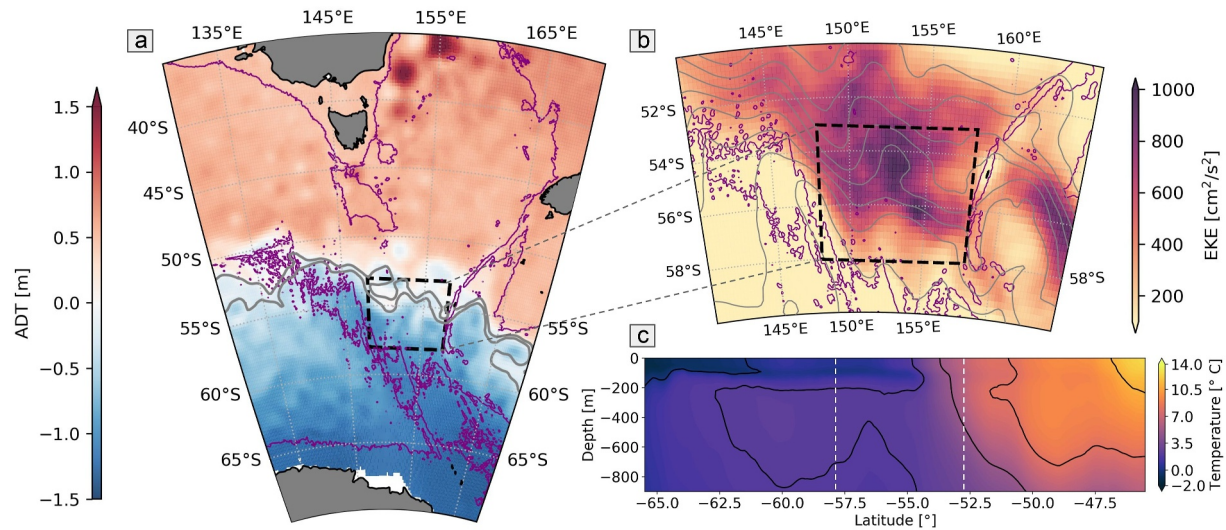


Figure 1. (a) CMEMS Absolute dynamic topography (ADT) average over 7 years (2015–2022) in the energetic Southern Ocean region between Tasmania and Antarctica. The purple lines represent the 3,000 m isobath, and the gray contours represent the Subantarctic Front (SAF) and the Polar Front (PF) taken from the CTOH/AVISO products. The black dashed line delimits the region of interest for the present study. (b) Average of DUACS dt2021 Eddy Kinetic Energy (EKE) from 1993 to 2022. The gray contours represent the SSH average from -1 to 1 m spaced by 0.2 m. (c) CMEMS vertical temperature section between 0 and 900 m, averaged over longitudes 148 – 158°E and between 2020 and 2021 between Tasmania 43°S and Antarctica 67°S . The black contours represent the 0°C , 2°C , 5°C , 8°C , 11°C isotherms. The white lines represent the latitude limit of the studied region.

established the strengths and limitations of the sQG vertical reconstruction in this complex dynamical region, we apply it to SWOT fine-resolution 2D surface geostrophic current field and to that from gridded conventional altimetry. We analyze two 5-day periods in March and October taken from a realistic coupled ocean-atmosphere simulation having a similar resolution to SWOT to assess the reconstructed dynamics in two contrasting seasons. This analysis is not intended to be a full quantitative representation of all the seasonal dynamics and variability in the region, which is beyond the scope of this work.

Section 2 provides some background on the region of interest, motivating its choice for this study. The data and methods are presented in Section 3. Section 4 includes the modeling study of the 3D dynamics of the region and the reconstructions of vertical velocity, temperature and vertical heat flux based on a realistic model. Section 5 offers an insight into the preliminary results on w reconstruction using SWOT SSH data, in preparation for a full validation with in situ data that will be part of a follow-up study. Finally, the conclusion and discussion are provided in Section 6.

2. Meso- and Submesoscale Dynamics in the Southern Ocean

The Southern Ocean is a critical region of the global ocean, with strong vertical heat and carbon uptake and exchanges with the atmosphere. Even though the Southern Ocean represents only 30% of the ocean surface, it accounts for 60% of the global heat content trend since 1970.

Within the Southern Ocean, the role of mesoscale to submesoscale eddy processes is critical. The meandering ACC promotes exchanges between the three ocean basins contributing to the global overturning circulation, which transports heat, moisture and carbon dioxide around the globe. The ACC also isolates cooler, fresher Antarctica waters from the warmer, saltier subtropical waters in the north. Watts et al. (2016) found that south of the ACC the ocean loses 0.4 PW of net heat to the atmosphere, and a large horizontal poleward oceanic heat flux is required to balance this loss. However, due to the zonal flow of the ACC, no strong meridional (N-S) mean currents carry this heat poleward in the upper $2,000$ m above the main bathymetric ridges. Instead, strong poleward heat fluxes are carried by mesoscale eddies across the ACC. These have been estimated from models (Boccaletti et al., 2005; Trenberth & Caron, 2001; Wolfe et al., 2008), from in situ moorings and altimetry (Foppert et al., 2017; Marshall et al., 2006; Phillips & Rintoul, 2000; Watts et al., 2016) and from Argo float observations (Sun et al., 2019). Mesoscale eddies also play a role in modulating the ACC dynamics (Sallée, 2018), and the Southern Ocean's eddy kinetic energy (EKE) evolves interannually (Martínez Moreno et al., 2020) and

contributes to the dynamical adjustment to climate variations (Hogg et al., 2008). Today, most of these Southern Ocean observational studies on the role of the horizontal transfers of heat, salt, carbon and nutrients come from large-scale Argo observations or altimetric currents that only resolve the large mesoscales. The role of horizontal stirring of fluxes at small mesoscales or submesoscales has been estimated only at localized sites (Jakes et al., 2024; Martin et al., 2001; Naveira Garabato et al., 2011; Nencioli et al., 2013) or from models (Le Sommer et al., 2011; Wolfe et al., 2008).

Recent studies show that the submesoscale also plays an important role. Su et al. (2020) found that the upper-ocean submesoscale produces a mean winter upward heat transport of more than 100 Wm^{-1} at latitudes of 60° , that is five times higher than the mean mesoscale heat transport, based on a high-resolution $1/48^\circ$ model. Compared to a lower resolution model, once the submesoscale is resolved, it contributes to warming the sea surface by up to 0.3°C and an annual air-sea heat flux anomaly of 10 Wm^{-2} . Submesoscale structures were initially thought to be confined within the mixed layer (Callies et al., 2015; Fox-Kemper et al., 2008) because of their assumed quasigeostrophic (QG) balance which would prevent the formation of strong density gradients at depth. However, recent modeling studies by Siegelman (2020) and Siegelman et al. (2020) have shown an enhanced vertical heat flux within deep submesoscale ocean fronts in the Kerguelen region in spring and summer, and Yu et al. (2019) found the largest submesoscale vertical velocities extending down to at least 200 m below the mixed layer base in winter and spring. Frontogenesis also penetrates from the ocean surface to below the ML base in the presence of deep fronts (Thomas & Ferrari, 2008). In addition to their dynamical role, Brannigan (2016) found that submesoscale resolving models present an enhanced biological activity in anticyclonic eddies that could lead to the upwelling of nutrient-rich waters and other biological activity within the eddies. Similar results arise with in situ observations. Using a combination of satellite altimetry and CTD data, Siegelman et al. (2020) reported vertical heat fluxes with a local amplitude reaching $2,000 \text{ Wm}^{-2}$ at the location of submesoscale fronts in the Kerguelen region, with vertical exchanges occurring both within and below the mixed layer (ML). The mechanisms we will focus on in this work are those driven by the vertical velocity from deep-reaching eddy stirring below the ML.

The area we analyze is located southeast of Tasmania (Figure 1), within a large meandering of the Polar Front. This is a region of energetic mesoscale and submesoscale dynamics (Foppert et al., 2017), downstream of the Southeast Indian Ridge (Cyriac et al., 2023). In this region, characterized by a topographic obstacle, standing meanders or lee waves are generated (Hughes et al., 1998) and many of the key physical processes central to the Southern Ocean heat and momentum balance are concentrated (Rintoul, 2018). Particularly, a poleward transport of heat (Meijer et al., 2022) and biogeochemical tracers (Patel et al., 2020) are generated by the strong mesoscale and submesoscale activity in the region, which makes the ACC “leak” (Naveira Garabato et al., 2011).

Numerous in situ data were collected here in late 2023, simultaneously with SWOT observations, in a collective effort for the calibration and validation of the satellite (d’Ovidio et al., 2019). In late 2023 the FOCUS campaign sampled the area at high resolution with a towed Triaxus, CTDs (conductivity, temperature, and depth), gliders, and deployed moorings (<https://www.swot-adac.org/campaigns/acc-smst/>). In the same period, as part of the Survostral campaign (<https://www.legos.omp.eu/survostral>), more than 400 expendable bathythermographs (XBTs) have been launched between Tasmania and Antarctica to sample the upper-ocean temperature structure at very high resolution (5–7 km) in the region of strong frontal activity. These data will be used in a more extensive validation of SWOT data, including for the vertical velocity and heat flux reconstruction in future work.

3. Data and Methods

3.1. Coupled Ocean Atmosphere Simulation (COAS)

Here, we use a new global coupled ocean-atmosphere simulation (COAS) at a km-scale resolution. COAS is generated by coupling the Goddard Earth Observing System (GEOS) atmospheric model to the Massachusetts Institute of Technology general circulation ocean model (MITgcm). For the atmospheric component, GEOS is configured to use the C1440 cubed-spheric grid, and a detailed description of the model configuration can be found in Molod et al. (2015). The atmosphere has a nominal horizontal grid spacing of 6.9 km and 72 vertical levels. The oceanic component uses the same configuration as the Latitude Longitude-polar Cap 2160 (LLC2160) simulation, detailed in Arbic et al. (2018), and is mesoscale and submesoscale permitting. We refer the reader to Torres et al. (2022) for more details on COAS and its validation. We solely analyze the ocean component,

configured with a nominal horizontal grid spacing of $1/24^\circ$ and 90 vertical levels with a non-uniform grid spacing of 1 m at the surface, increasing to around 300 m at the bottom and tidal forcing. The simulation period covers 14 months, from 20 January 2020 to 25 March 2021, with the first 2 months corresponding to the spin-up period. The LLC2160 also includes an hourly forcing of the full lunar-solar tidal potential (Arbic et al., 2018). This triggers the generation of internal tides and allows for a more realistic seasonal study. The validation of the LLC2160 has been performed by Rocha, Gille, et al. (2016) blue with the following analysis: comparing the model's near-surface velocity field against two available mooring data records in the Kuroshio Extension shows a good agreement. A global comparison with an ARGO climatology shows that the upper ocean stratification and seasonal variability are well captured in the LLC2160 simulation. Model fields show eddy kinetic energy (EKE) levels similar to Jason II and gridded altimetry maps when smoothed over similar scales. Finally, they have compared the LLC2160 SSH variance and surface kinetic energy spectrum to the well-known LLC4320 simulation and show indistinguishable values between 20 and 100 km (the scales of interest for our study).

In this demonstration study to test the vertical sQG reconstruction, we extract two 5-day periods in contrasting seasons, 25–29 March 2020 and 25–29 October 2020. In the study region, the resolution of $1/24^\circ$ corresponds to an average grid point of 2.3 km, comparable to the SWOT basic ocean product's 2 km grid. Although other simulations exist with higher resolution (e.g., LLC4320 at $1/48^\circ$ (Rocha, Chereskin, et al., 2016)), COAS' horizontal resolution at our latitudes is sufficient to capture the physical features of interest for our study and its observation with SWOT. In addition, COAS's weaker (and more realistic) tidal forcing compared to LLC4320 allows for better comparison between model outputs of w and reconstructed w .

3.2. Effective Surface Quasi Geostrophic (sQG) Theory

Surface quasi-geostrophic (sQG) theory used in this work is the “effective” version defined by Lapeyre and Klein (2006). It is based on the reduction of Eady's model for baroclinic instabilities from one boundary (here the ocean surface), used to describe the oceanic mesoscale eddy fields in the surface layers (Klein & Lapeyre, 2009). This approach is valid for the surface intensified eddies. The reconstruction of other eddies, namely subsurface intensified eddies, requires the combination of the effective sQG with the interior sQG (iSQG) as in Wang et al. (2013), where both have a signature in SSH. The major assumption for effective sQG is that potential vorticity (PV) is uniform and constant in the ocean interior. Using PV inversion, one can retrieve a geostrophic stream function (ψ) related to PV using an elliptic operator (Klein et al., 2009). Following Klein et al. (2009) and assuming a doubly periodic domain, the geostrophic stream function is retrieved at all depths (z) from SSH (η) using an exponential decay as:

$$\hat{\psi}(\mathbf{k}, z) = \frac{g}{f} \hat{\eta}(\mathbf{k}) \exp\left(\frac{N_0}{f} kz\right) \quad (1)$$

where $\widehat{(\cdot)}$ corresponds to the Fourier transform, $\mathbf{k} = (k_x, k_y)$ is the wavenumber vector and $k = |\mathbf{k}|$ is its norm, g is the gravity constant, f is the Coriolis frequency, N_0 is a Brunt-Väissälä frequency that accounts for the contribution of the interior PV. Vertical motions are retrieved from the buoyancy equations as in Klein et al. (2009).

$$\hat{w}(\mathbf{k}, z) = -\frac{c^2}{N_0^2} \left[-J(\widehat{\psi_s}, b_s) \exp\left(\frac{N_0}{f} kz\right) + J(\widehat{\psi}, b) \right] \quad (2)$$

where the subscript s refers to the surface values, b is the buoyancy, c is a unitless constant that helps optimize the reconstructed fields' amplitude and $J(A, B) \equiv (\partial_x A \partial_y B - \partial_y A \partial_x B)$. This methodology requires the optimization of the constants N_0 and c . We refer the reader to Lapeyre (2017) for a full derivation of sQG theory.

Following Klein et al. (2009), the SSH field is filtered in space before applying sQG. We apply a two-dimensional Lanczos low-pass filter in the spectral domain to eliminate all wavelengths smaller than 20 km (Duchon, 1979). The reconstructions obtained with the filtered SSH are compared to the COAS fields also filtered with the same method. This choice derives from the study of Klein et al. (2009), who assesses that sQG is non-realistic below these scales. This is confirmed by comparing the COAS and sQG vertical velocity wavenumber spectra before the 20 km filter is applied (not shown), revealing a clear drop in energy in the sQG w reconstruction at scales smaller than 20 km at the surface and at larger scales at depth. To reduce the residual noise from the SWOT data due to

surface waves and other perturbations (Tréboutte et al., 2023), the same filter is later applied to the SSH fields of SWOT before application of sQG, ensuring consistency with the model results. We estimate that 20 km is a reasonable scale to match the effective capability of the gridded SWOT product.

In this study, since we have access to the full model vorticity and velocity field, we optimize N_0 so that the shape of the model and sQG vorticity rms has a minimal mean squared error from the bottom of the mixed layer to 1,000 m. The mixed layer average is around 100 m in March and 250 m in October over the full domain. The optimal N_0 for this domain is $3.72e - 6 \text{ s}^{-1}$ in March and $3.98e - 6 \text{ s}^{-1}$ in October. We keep separate values to reproduce the seasonality of the vertical stratification. With these values, the correlation between the COAS and sQG vorticity fields is around 0.9 for the full water column (not shown).

To optimize c we work directly with the density anomalies and w fields, having an SSH filtered at 20 km before applying sQG and obtaining one optimal parameter c for the density anomaly reconstruction and one for the vertical velocity for each season. For the optimization, following Klein et al. (2009), we aim to align the maximum amplitudes so that, on average, the difference between the 2D COAS and the reconstructed physical fields between the bottom of the mixed layer and 1,000 m is minimized. First, the model density anomaly and w corresponding to the maximum amplitude values of magnitude occurring outside 1σ are extracted. This selects 30% of density anomaly points in March and 35% in October for each vertical layer on the water column and 23% (March and October) for the vertical velocity. We find an average optimal c of 1.2 for the vertical velocity and 1.51 for the density, which applies to both seasons.

We use various diagnostics to assess the quality of the sQG reconstruction. These include the 5-day average of the spatial correlation of the physical parameters between the COAS and the sQG fields and the vertical profile of average rms values for each depth. Wavenumber spectra at different depths are used to quantify which scales are well represented and where we lose the spectral energy, identifying those scales where the sQG reconstruction is ineffective in representing the dynamics.

3.3. Reconstruction of Temperature Anomalies

In order to calculate vertical heat fluxes, we need to know the vertical profile of temperature anomaly. In this work, we investigate the use of temperature anomalies retrieved from two different sources: from a pseudo-gridded product from observational data (Section 3.3.1) and from a sQG reconstruction of density anomalies (Section 3.3.2).

3.3.1. Temperature Anomalies From an Observational Gridded Product

We test the computation of the VHF with temperature anomalies based on existing 3D gridded temperature-salinity products like ARMOR 3D (Guinehut et al., 2012). This product is built by merging widely spaced in situ observations of temperature and salinity (XBTS, CTDs, moorings and Argo profiles) with remote sensing observations of sea level anomaly and sea surface temperature (Barceló-Llull et al., 2018). The operational product provides weekly 3D temperature, salinity, geopotential height and geostrophic currents globally on a $1/4^\circ$ grid. It has been validated by Mulet et al. (2012) against model reanalysis and in situ observations (ANDRO current velocities from Argo float displacements and velocity measurements from the RAPID-MOCHA current meter array). The effective resolution at our latitudes is around 150 km, comparable to the DUACS altimetry products (Ballarotta et al., 2019). For the sQG reconstruction assessment against the full model in Section 4, we mimic the ARMOR temperature product by filtering COAS simulation temperature fields to remove all wavelengths smaller than 150 km. The product, referred to as “pseudo-ARMOR” temperature, is then used for the computation of the sQG reconstructed VHF. In Section 5 the reconstructed SWOT or conventional altimetry VHF are retrieved using the real ARMOR 3D temperature fields. More details can be found in Appendix B. In all cases, the temperature anomaly is computed spatially, with respect to the original field linearly detrended in longitude and latitude.

3.3.2. Temperature Anomalies From sQG Density Anomalies

In some applications, we could be interested in computing the VHF only using satellite altimetry. In this case, temperature anomaly can be reconstructed from the sQG density anomaly by constructing a linear regression between the model temperature and density for each depth level. For this study, one regression is built for each

vertical layer and season, and it is used to reconstruct the temperature anomaly profiles from the 3D sQG density anomalies. The regression is stable in time over the 5 days for each season. The temperature anomalies computed with this method are then used for the computation of the reconstructed VHF. In this frontal region, we test the dominance of temperature or salinity in determining the density field structure and tune the regression for values below the mixed layer above 1,000 m. In March and October, the temperature gradients dominate the density gradients above 600 and 800 m, respectively. Below these levels, the temperature derivation is less accurate. The strengths and drawbacks of the method are discussed in Section 6 along with alternative methods to retrieve temperature profiles from high-resolution SSH observations. The details of this methodology are given in Appendix A.

3.4. Vertical Heat Fluxes (VHF)

VHF are computed following Su et al. (2018) and Siegelman et al. (2020) as $VHF = \rho_0 C_p w' T'$, with $\rho_0 = 1,023 \text{ kg m}^{-3}$ the reference seawater density, $C_p = 3,985 \text{ J kg}^{-1} \text{ K}^{-1}$ the specific heat capacity of seawater, w' the vertical velocity, T' the temperature. The prime refers to the spatial anomaly of the linearly detrended 2D domain averaged values for each vertical layer. Positive (negative) values indicate an upward (downward) flux. VHF from COAS are computed with the filtered (with the low-pass filter of 20 km introduced in Section 3.2) outputs of vertical velocities and temperature, consistent with the vertical velocity field mentioned above. VHF reconstructions are computed with sQG vertical velocities and with temperature anomalies either from the pseudo-ARMOR product or from sQG reconstruction, as detailed above. As for the vertical velocity reconstruction, diagnostics of the reconstructed VHF in the two cases are compared with VHF derived from COAS, using 2D spatial correlations and spatial rms for each layer of the water column to assess the quality of the VHF reconstructions.

4. Model sQG Reconstruction Assessment

All the results presented in this section are obtained using COAS simulation outputs. First, we investigate the main dynamical structures present in the region of the energetic Polar Front south of Tasmania. Second, we reconstruct vertical velocities and vertical temperature anomalies using SQG theory. Third, we build a pseudo-ARMOR temperature product to compute the heat fluxes. Finally, we derive vertical heat fluxes from vertical velocities and temperature anomalies. This section serves as a foundation for Section 5, which uses SWOT observations to reconstruct these same quantities.

4.1. Dynamical Properties of the Study Region South of Tasmania

The study region is the energetic EKE hot-spot of the Antarctic Circumpolar Current (ACC) southeast of Tasmania (Figure 1a), extending North and South of the local Polar Front (PF) (Dong et al., 2006). This region has strong EKE, reaching over $1,000 \text{ cm}^2 \text{ m}^{-2}$ on average over the last 30 years (Figure 1b). Large mesoscale eddies have been tracked crossing the front, cold-core eddies transport cold water from south of the front, and vice versa for warm-core eddies: both contributing a strong poleward heat transport (Morrow et al., 2004; Patel et al., 2019). Recent studies have also highlighted the important vertical velocities generated in such regions, leading to enhanced upwelling of Circumpolar Deep Water around the major topographic Southern Ocean features such as Southeast Indian Ridge or the Macquarie Ridge around 160°E (Tamsitt et al., 2017).

The interaction of multiple mesoscale and submesoscale eddies contributes to the formation of strong horizontal velocity gradients. Figure 2 shows COAS modeled fields at a selected hourly snapshot on 29 March 2020 (the October fields show very similar results and are therefore not shown) for (a) relative vorticity ($\zeta = v_x - u_y$ with the subscript x of y referring to the derivative of the variable along the x , y direction), (b) the strain rate ($\sigma = \sqrt{\sigma_n + \sigma_s}$ with $\sigma_n = u_x - v_y$ the normal strain and $\sigma_s = v_x + u_y$ the shear strain rate), at 250 m depth and their distribution at different depths. These diagnostics give insight into the dominant dynamics in the region, and how they extend in the water column. The sign of the relative vorticity in Figure 2c is used to separate cyclones (negative) and anticyclones (positive) (Frenger et al., 2015). Filaments of vorticity have a larger positive skewness than vortices due to ageostrophic frontogenesis (Siegelman et al., 2020). The COAS fields show positive skewness indicating strong vorticity filaments down to 1,000 m for both seasons (skewness is quite similar at all depths in March, 0.39, 0.41, 0.47, 0.37 from the shallowest to the deepest, slightly decreasing in October, 0.66, 0.66, 0.72, 0.57). Regions of strong strain in Figure 2d are of interest as they lead to the formation of

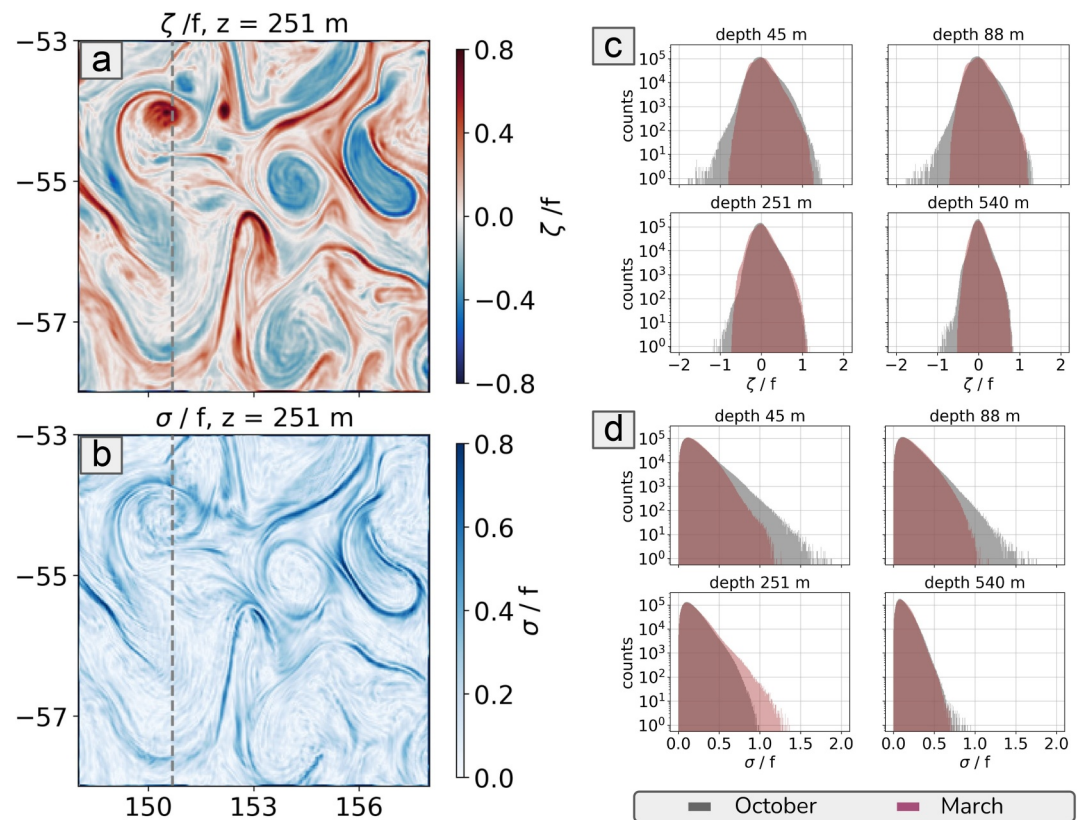


Figure 2. COAS snapshots of (a) relative vorticity divided by f and (b) strain rate divided by f , with f the Coriolis parameter at 00UTC on the 29th of March. Distributions of (c) relative vorticity divided by f and (d) strain divided by f at 45, 88, 251, and 540 m for all hourly snapshots over 5 days in March (25th–29th; brown shading) and October (25th–29th; gray shading). The gray dashed line at 151°E in (a) and (b) represents the longitude at which the vertical profiles are taken throughout the paper.

strong horizontal gradients of buoyancy, or fronts, which cause the development of vertical velocities (Hua & Klein, 1998). Both the vorticity and the strain rate show strong filaments and fronts with a magnitude close to the Coriolis frequency f , especially in the first 100 m, highlighting the energetic variability of this region, consistent with the strong EKE shown in Figure 1. In October the distribution shows high values of vorticity and strain in the upper ocean, especially within the October average mixed layer of 250 m. Regions of strong strain at the edge of the eddies are also regions where strong horizontal buoyancy gradients develop (Figure 3) along the full water column.

Vertical sections from the model reveal complex dynamical features in the ocean interior. Figure 3 shows the vertical extension of mesoscale eddies below the mixed layer (ML). Here, the mixed layer depth (MLD) is chosen where the density increases of 0.03 kg m^{-3} with respect to the density at 7 m depth (de Boyer Montégut et al., 2004). The average MLD in the region for the selected dates is 103 m in March (late summer/early autumn) and 250 m in October (late winter/early spring). We show a transect at a longitude of 151°E down to a depth of 1 000 m because it crosses specific eddy structures of this region (see dashed line in Figures 2a and 2b), with different characteristics. A large eddy develops from the surface down to 1,000 m south of 54°S, and has a strong positive signature in vorticity and a strong horizontal buoyancy gradient $|\nabla b|$. Smaller eddies north of 54°S or south of 55°S are trapped in the subsurface and develop down to 500 and 300 m. They have a strong signature of buoyancy anomaly b' in their core and a strong horizontal buoyancy gradient at their edge. This vertical section also shows internal wave structures at depth, which may not entirely be reconstructed with the sQG methodology.

Indeed, a major question for the vertical sQG reconstruction from SWOT data concerns the impact of residual high frequency dynamics on the SSH, from internal tides or these internal gravity waves. Our COAS model SSH fields include tides and internal tides that have not been corrected due to the short 5-day time series. SWOT and

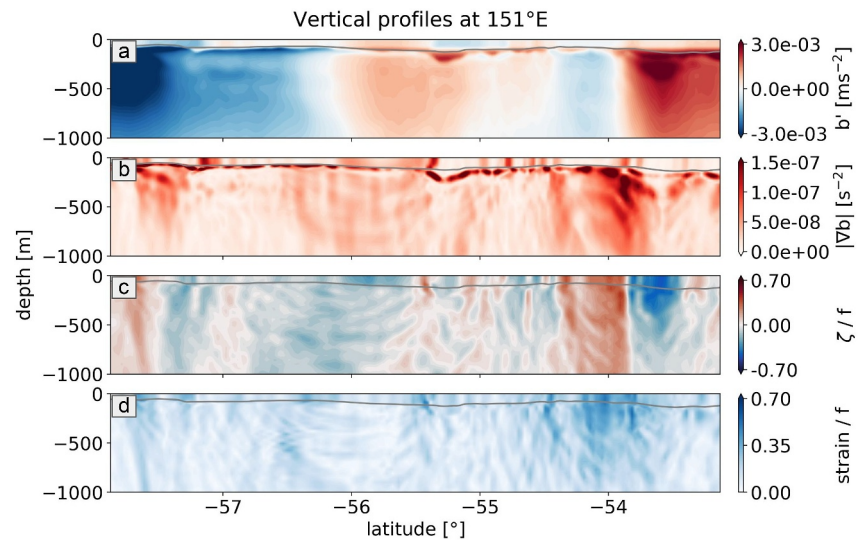


Figure 3. COAS vertical profiles over the first 1,000 m at 151°E of (a) buoyancy anomaly b' , (b) magnitude of the horizontal buoyancy gradient $|\nabla b|$, (c) normalized vorticity, (d) normalized strain rate, from one hourly COAS snapshot at 00UTC on the 29th of March. The gray contour is the average mixed layer in the region over 5 days.

conventional altimetry surface fields are corrected for the barotropic tides and the main phase-locked internal tides Dibarboure et al. (2024), but not for the incoherent internal tides. So, it is instructive to see how the sQG formalism deals with these high-frequency signals, even if they are more energetic in the model than in the corrected SWOT SSH fields. To check this, we have calculated wavenumber-frequency spectra for the full COAS w and the sQG reconstructed w fields, using the hourly outputs for the 5 days of available data in March at 250 m depth (below the mixed-layer). Figure 4a shows that the full COAS simulation (without any correction for the tidal signal) has very energetic high frequency w over multiple wavelengths above the 20 km cutoff set for the sQG reconstruction at the inertial frequency f , at the major M2 tide frequency and higher tidal harmonics, and cascading to smaller space and time scales. We expect large amplitude internal waves or inertial oscillations to have a much smaller signature at the surface. Figure 4b shows that the sQG formalism effectively dampens most of this high-frequency energy but some residuals remain in the reconstructed w fields. We expect that the corrected SWOT SSH data will have even less energy at tidal frequencies in SSH and therefore in the reconstructed w fields. In the following assessment of the sQG reconstruction, we use daily averaged SSH data before applying the sQG (white dashed line in the plots); this step removes even the residual high-frequency energy from the reconstructed fields. This daily average is not possible with SWOT snapshots, and SWOT SSH fields might include some weaker residual high-frequency energy. This will be discussed in Section 5.

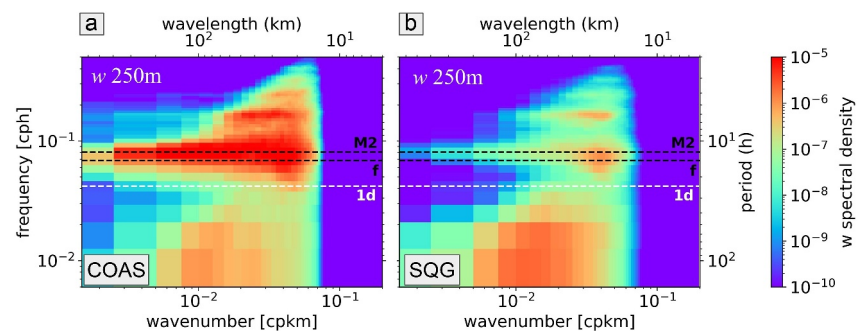


Figure 4. Vertical velocity power spectral density at a depth of 250 m computed with (a) the COAS simulated w lowpass filtered at 20 km and (b) the sQG w from the COAS lowpass filtered SSH at 20 km. Figures refer to the hourly data over 5 days from March 25th to 29th.

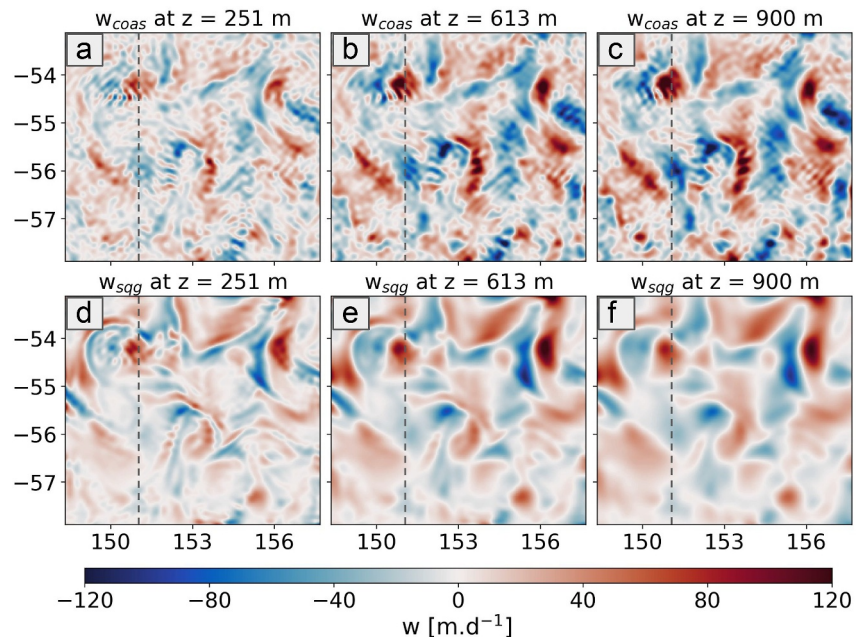


Figure 5. Vertical velocity from the COAS simulation for depths of (a) 250 m, (b) 613 m, and (c) 900 m. Vertical velocity sQG reconstruction at (d) 250 m, (e) 613 m, and (f) 900 m. The gray dashed line in (a) represents the longitude at which the vertical profiles are taken in Figure 3. Figures (a)–(f) refer to the daily averaged outputs on the 29th of March 2020.

4.2. Vertical Velocity Reconstruction

Once the stratification and amplitude parameters are optimized, the sQG methodology is applied to reconstruct vertical velocities in the domain for both seasons, using daily averaged COAS SSH. The physical sQG fields in Figure 5 show that the small eddy structures are present below the mixed layer at 250 m, and become progressively smoothed at depth. The 2D geographical fields of the COAS and sQG vertical velocity at three different depths are represented in Figures 5a–5f. sQG can reconstruct some of the small-scale eddy structures closer to the surface, see Figure 5d at 251 m between 54°S and 55°S for instance, but these features are gradually smoothed out with depth in the sQG reconstruction, in Figures 5e and 5f. sQG does not reconstruct the small wave-like instabilities in the COAS simulation at each depth. The correlation remains consistently around 0.6 at all depths below the mixed layer, representing the mesoscale and large submesoscale filaments. The reduced energy in the reconstructed vertical velocities at depth is also quantified by the vertical profiles of rms in Figure 7d.

Vertical sections of the COAS versus sQG w fields are shown in Figures 6b and 6c, and highlight one of the key aspects of this region—the vertical velocities in COAS are stronger at depth, in this regions of strong bathymetric control downstream of a major ridge, as noted by Tamsitt et al. (2017). Above 500 m, the sQG shows some of the small-scales variability that is gradually filtered at depth. The COAS features at depth are large-scale structures with a large SSH signature. In fact, the vertical profile between 53°S and 54°S shows that while the COAS simulation has an inversion of velocity around 500 m, the sQG projects the surface dynamics to the ocean interior. South of 54°S there is a large ascending w hotspot colocalized with a large horizontal buoyancy gradient and vorticity (Figures 3b and 3c). This feature is captured by the SSH and projected by the sQG exponentially at depth, since the sQG, by construction, is not able to represent the increasing amplitude at depth. This is highlighted by the difference between the COAS and sQG fields (Figure 6d). In fact, in this specific transect, the sQG explains up to 90% of the signal in the first 500 m gradually decreasing to 50% at 1,000 m. The case at 56°S is different, where we find a negative (downwards) w hotspot whose sign is captured by sQG, whereas the amplitude is underestimated. This corresponds to a region where the SSH gradients (Figure 6a) are weaker, which explains the magnitude misfit in the reconstructed w , especially since it develops from the bottom. The difference between the two fields is in the order of half of the COAS w value, underlining a limitation of the sQG model. South of 57°S the main difference between the two fields is due to some rapidly changing (20–30 km) vertical velocity structures that cannot be effectively represented by the sQG reconstruction because of their small scale. The specific

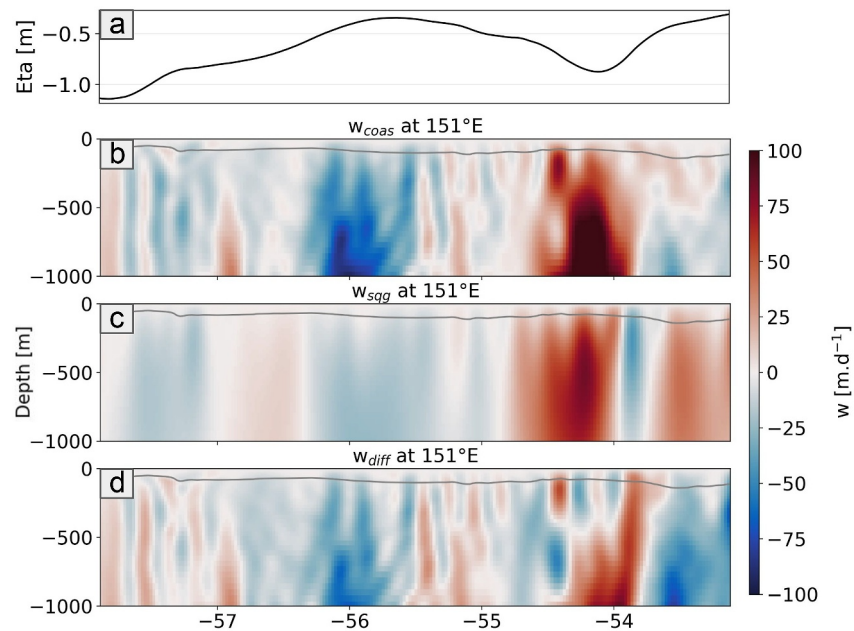


Figure 6. (a) COAS SSH profile at 151°E. Vertical profile of (b) COAS, (c) sQG vertical velocity and (d) their difference at 151°E, where the x-axis is the latitude [°S], on the 29th of March. The gray contour corresponds to the average mixed layer (ML) in the region for the 5 days between March 25th and 29th.

processes involved in the w intensification at depth observed in the model are not studied in detail, the contribution could come from the enhanced dynamics downstream of the Southeastern Indian ridge, wave effects, or different instabilities from the flow fields. What stands out from Figures 5 and 6 is that if these instabilities in the ocean interior have a signature in SSH (e.g., south of 54°S), they are picked up and projected at depth by the sQG, with the correct intensity for the first 500 m and underestimated up to 50% below. The effective sQG cannot reconstruct other dynamical features and a more sophisticated representation of the ocean interior would be necessary for this purpose. This means that in such an energetic region in the presence of these dynamics, we might be missing part of the transport of heat between the ocean interior and the surface.

The spatial scales being resolved are quantified by the wavenumber spectra for the COAS and sQG reconstructed w fields at two different depths in March, shown in Figure 7a, characterized by a relatively good spectral energy of the two fields at large scales at these two depths. At 251 m depth, the sQG w clearly shows a reduction in energy at scales <30 km; at 613 m depth, the sQG starts losing energy below 70 km, underestimating smaller scales.

Figure 7b shows spectral coherence for each depth. Although scales larger than 70 km have similar spectral energy (Figure 7a), they are less coherent over the full depth range. As shown in Figure 3, the large scale sQG w energy is projected from the surface downward, whereas the COAS w is often depth-intensified. Although the sQG w has reduced spectral energy at scales smaller than 50–70 km, it has the highest w spectral coherence. The spectral coherence remains above 0.5 for scales between 30 and 60 km for the full water column, slightly decreasing with depth. This is in line with the 2D fields of Figure 5 which show that the sQG field at depth is smoothed compared to 250 m, but some of the large mesoscale structures (~50 km) are resolved with a lower magnitude (see the rms at depth Figure 7d).

The sQG reconstruction is evaluated in terms of the spatial correlation between the COAS and sQG w field, and their associated rms. Figure 7c shows that spatially the structures are well localized, with a spatial correlation reaching 0.6 for the full water column, both in March and October, in line with other sQG reconstructions in the Pacific Ocean (Qiu et al., 2020). At the surface the result is not exploitable down to the bottom of the ML, indicated by the shaded gray sections (darker gray for the shallower ML in March, lighter gray for the average ML in October). The rms (Figure 7d) is comparable between sQG and COAS in the top 300 m (400 m) in March (October), although the sQG has slightly higher values than COAS in the first 200 m (300 m). Below 400 m, the sQG rms slightly decreases but maintains w rms values of around $25 \text{ m} \cdot \text{d}^{-1}$ in both seasons, which is lower than

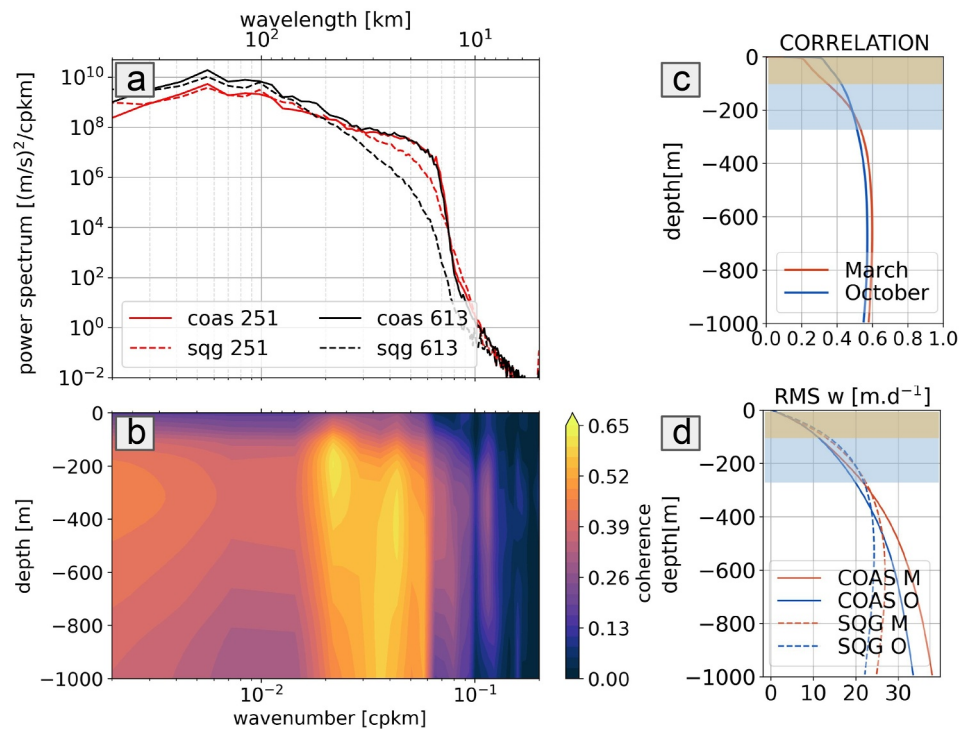


Figure 7. (a) Wavenumber spectrum of COAS (filtered at 20 km) and sQG vertical velocity at 251 and 613 m on March 29th. (b) Spectral coherence between the COAS and sQG field for each depth. (c) Spatial correlation between the COAS and sQG vertical velocity fields for each depth. (d) Rms of the COAS and sQG vertical velocity fields. The shading corresponds to the average mixed layer (ML) in the region for the 5 days between March 25th and 29th (orange), and between October 25th and 29th (blue).

COAS by 15 md^{-1} and 10 md^{-1} respectively in March and October at 1,000 m. This means that on the overall field, the SQG reproduces up to 70% of the COAS rms at depth. Note that, as in Klein et al. (2009), the sQG diagnosed vertical velocity rms does not present any local maximum close to the bottom of the ML. This feature is also absent in the filtered version of the COAS vertical velocity rms, but present in the non-filtered version (not shown). This is likely to be due to the sQG lack of representing ML dynamics and Ekman pumping at the bottom of the ML.

4.3. Temperature Anomalies Reconstruction

We consider two techniques for estimating fine-scale temperature fields in order to calculate VHF. The first is the pseudo-ARMOR gridded product for the temperature anomaly, and the second is the temperature anomaly derived from the sQG density anomalies by linear regression (see Section 3.3.2). Both temperature anomalies are illustrated in Figure 8 compared with the full-model COAS temperature anomaly. An example of the 2D geographical fields at 250 m depth (Figures 8a–8c) shows that the small-scale structures in the temperature anomaly are smoother in the pseudo-ARMOR case but with similar polarity, whereas the sQG temperature reconstruction has larger amplitude anomalies, but sometimes of the wrong sign. The diagnostics over the entire region and at depth confirm this. The spatial correlation of the full COAS temperature anomaly with the reconstructed temperature fields (Figure 8g) indicates that these large-scale structures in the pseudo-ARMOR field are well positioned (correlation ~ 0.9 along the full water column). Whereas the sQG temperature reconstruction has a lower correlation (0.8 at the surface decreasing to 0.6 at depth) since specific structures and vertical water mass distributions (see Figures 8e and 8f at 57°E compared to Figure 8d) are not reconstructed by the sQG theory.

The full model rms (Figure 8h) is closer to the sQG case than the smoother pseudo-ARMOR reconstruction below the mixed layer. The sQG rms (Figure 8h) below the ML presents a good agreement with the COAS temperature, with a slight underestimation of 15% in March up to 600 m and 20% in October up to 800 m (not shown) with

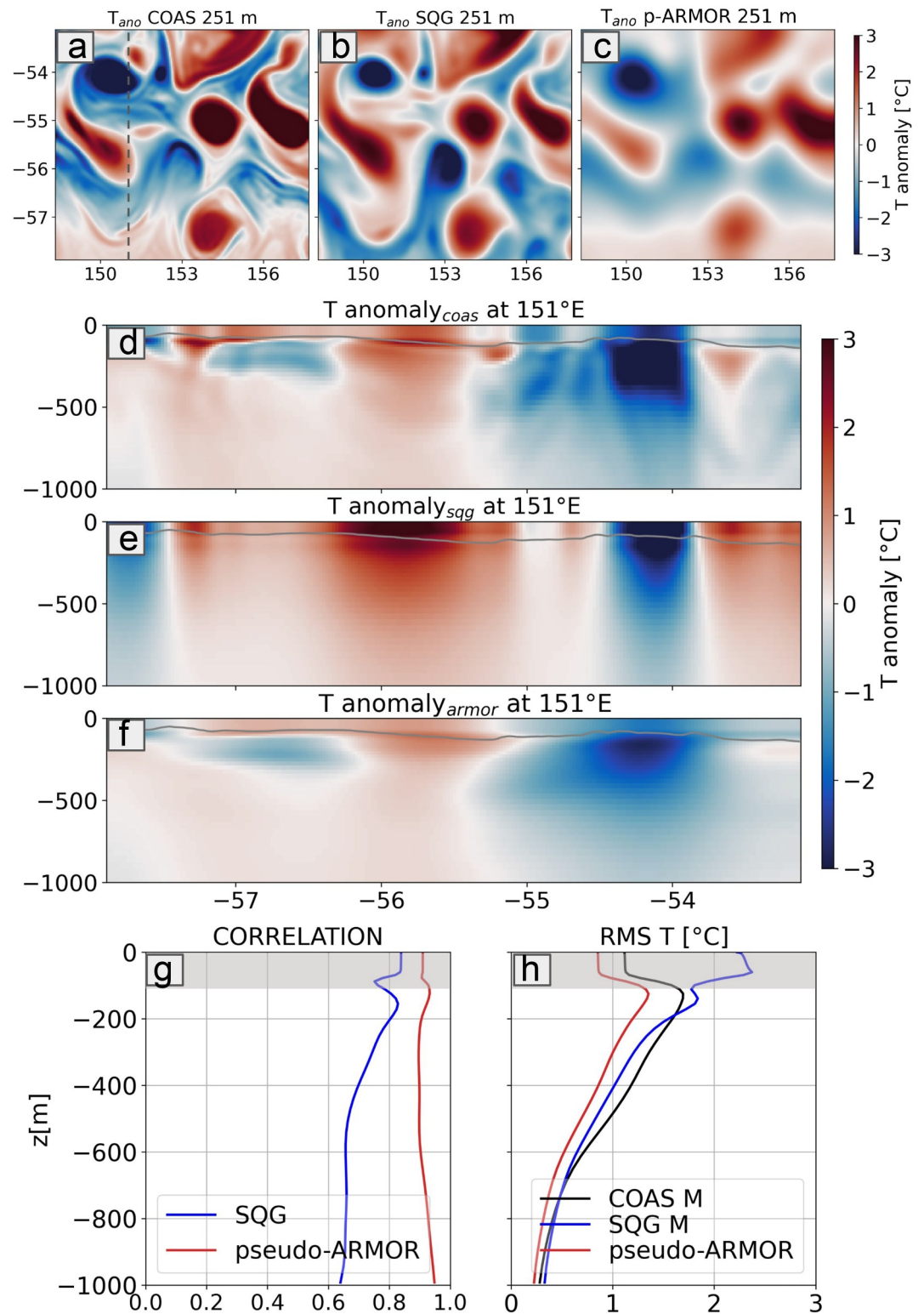


Figure 8. (a–c): 2D temperature anomaly from the COAS simulation, the sQG reconstruction and the pseudo-ARMOR product, respectively. (d–f): vertical temperature anomaly profile at 151°E for the from the COAS simulation, the sQG reconstruction and with the pseudo-DUACS product, respectively. (g) Spatial correlation between the full COAS simulation and the sQG reconstruction (blue) and the pseudo-ARMOR field (red). (h) Rms of the three fields at each depth. The gray shading is the average mixed layer depth in March. Figures refer to the daily averaged outputs on the 29th of March 2020.

respect to the reference anomalies. Below, the temperature anomalies are well aligned. The pseudo-ARMOR temperature differs from the sQG reconstruction by an extra 15% in rms between 200 and 600 m and up to 30% at 1,000 m. Thus, even if the large-scale structures are spatially better represented in the pseudo-ARMOR field, the missing small scales (<150 km) are bringing much of the variability in the temperature anomaly. Different studies using ARMOR 3D have pointed out the underestimation of inferred QG vertical velocities (Barceló-Llull et al., 2016; Mason et al., 2017; Pascual et al., 2015), due to the smoothing of the field. Within the ML, the sQG temperature anomaly rms presents a large departure from the modeled one (~100% at the surface), which would prevent any interpretation of the results in this layer. The pseudo-ARMOR temperature anomalies are closer to the correct ML structure, with a lower magnitude, overall between 25% and 30% lower than COAS along the full water column.

The comparison of Figures 8e and 8f show one of the limits of the sQG methodology for reconstructing temperature anomalies: while the large-scale structures are well represented and aligned with the modeled ones, sQG is not able to represent all the water mass structure in the mixed layer and at the bottom of the mixed layer. Between 56°S and 57°S, for instance, the negative temperature anomaly is not reproduced, and the full sQG water column has a positive temperature anomaly. In some cases, the sQG anomaly has an opposite sign next to the boundaries (e.g., south of 57°S because it projects the surface negative anomaly at depth). The pseudo-ARMOR product (Figure 8f) keeps the large-scale temperature variability along the water column and the distinct water masses that exist north and south of the polar front.

4.4. Vertical Heat Fluxes Reconstruction

After reconstructing the vertical velocities and temperature anomalies in the first 1,000 m of the water column, we can estimate the amount of vertical heat flux that this methodology can capture compared to the COAS simulation taken as a reference for the study. Figure 9 shows the full COAS model VHF compared to the two reconstructed VHF, both computed with sQG vertical velocity but either using the pseudo-ARMOR temperature or the sQG reconstructed temperature. The 2D fields (Figures 9a–9c) show that the two reconstruction methodologies for computing the VHF give similar results in terms of reconstructed structures, highlighting that the sQG vertical velocities are the key factor for the VHF. As for the vertical velocities, the small-scale COAS wave patterns are not reconstructed with sQG.

The vertical sections along 151°E (Figures 9d–9f) show a large eddy strain driving downwelling around 54°S in COAS, that is well captured by the two reconstruction methodologies. In contrast, north of 54°S, COAS shows a small sub-surface-trapped eddy inducing upwelling in the COAS VHF that is not captured by either of the correlations. The COAS temperature (Figure 8) shows this eddy below the mixed layer extends down to 400 m, but pseudo-ARMOR resolution is too coarse to retain it, and the sQG temperature reconstruction projects it from the surface to depth. These two examples highlight that the reconstructed VHF only presents the major coherent structures given by the w sQG on the full vertical column. Although, in regions south of the polar front like between 56 and 57°S the pseudo-ARMOR temperature reconstruction allows for a representation of some vertical structures in the VHF.

The correlation (Figure 9g) shows a similarity between the sQG and the pseudo-ARMOR reconstructed VHF down to a depth of 700 m. Between 700 and 1,000 m, the sQG w field represents large spatial scales, but the sQG temperature reconstruction has reduced correlation (Figure 8g), resulting in a reduced sQG reconstructed VHF correlation at depth (<0.1 less than the pseudo-ARMOR reconstruction) at 1,000 m. However, due to the smoother reconstructed temperature, the pseudo-ARMOR case has a lower rms (Figure 9h, around 40% at 200 m and around 10% at depth). North and south of the meandering polar front region with its energetic, deep-reaching eddies, the pseudo-ARMOR temperature anomaly does a better job representing the vertical water masses layers in the upper water column, and the dynamics within and below the ML are better represented than with the sQG reconstruction. However, Figure 9h indicates that overall on the vertical heat fluxes, the rms is dominated by the contribution of the vertical velocity; recall that the sQG reconstructed vertical velocity underestimates the full COAS model below 600 m by 30%–40% (Figure 7d). Thus, improving the w reconstruction is paramount for a better representation of the VHF.

Thus, the reconstruction using the sQG w and temperature and the one using the sQG w and the pseudo-ARMOR product give comparable statistical results in terms of VHF structures, albeit with improved correlation of the vertical structures with the pseudo-ARMOR temperature reconstruction over all depths, but with an overall better

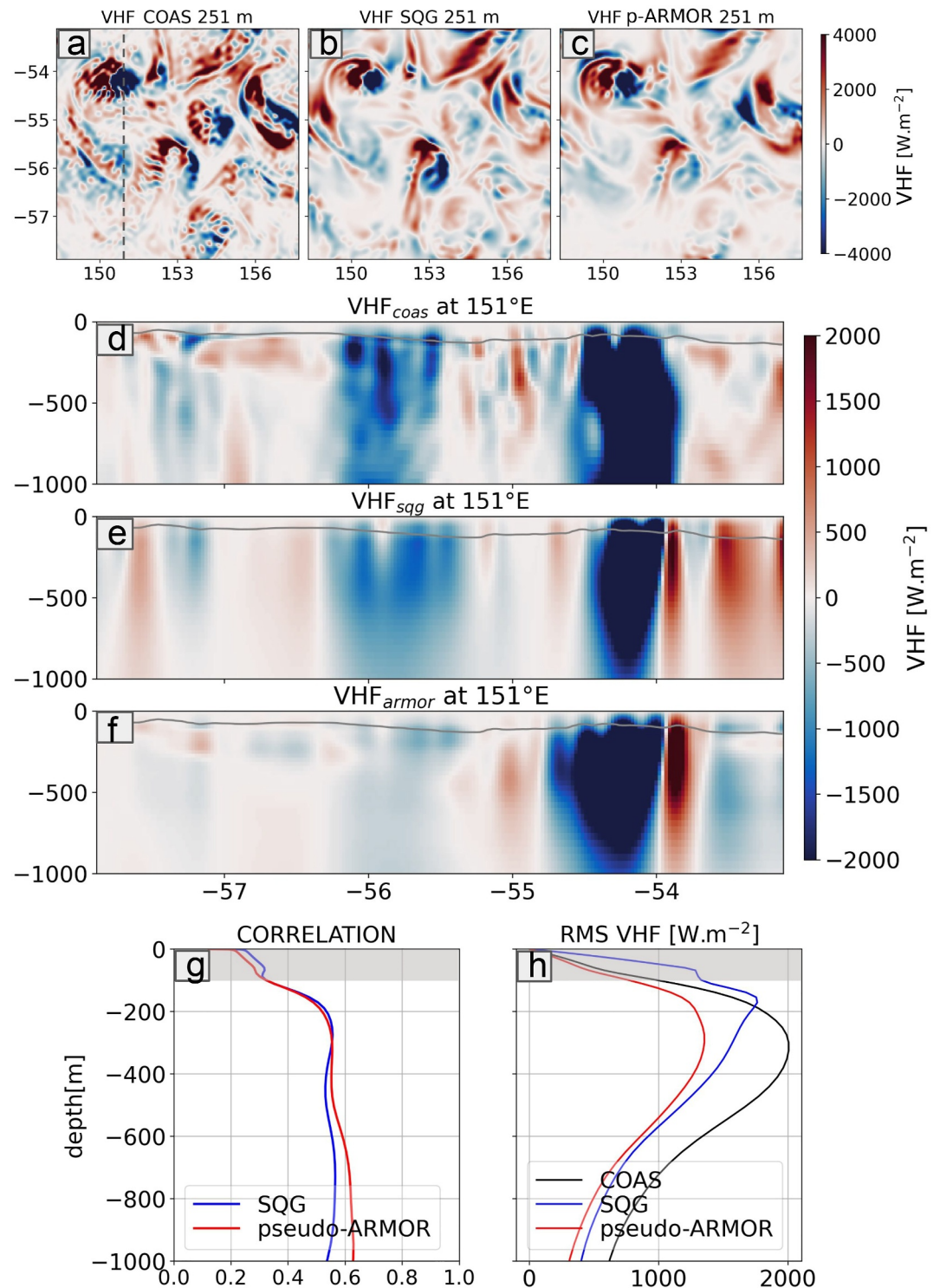


Figure 9. Vertical heat flux for the 2D field in the (a) full model w and T , (b) sQG w and T reconstruction, (c) sQG w and pseudo-ARMOR reconstructed T field. (d) Spatial correlation between the full COAS simulation and the sQG reconstruction (blue) and the pseudo-ARMOR field (red). (e) Rms of the three fields at each depth. The gray shading is the average mixed layer depth in March. Figures refer to the daily averaged outputs on the 29th of March 2020.

rms below the mixed layer provided by the full (w and temperature) sQG reconstruction. These results suggest that the existing operational gridded temperature products like ARMOR 3D could be used to retrieve VHF associated with mesoscale structures down to 1,000 m and offer promising results, especially within the ML where the sQG performs worse. This methodology is a good alternative to the sQG reconstruction, especially in regions where a tight linear regression between density and temperature necessary for the sQG reconstruction cannot be correctly estimated.

5. SWOT-Derived Vertical Velocities and Vertical Heat Fluxes

This section presents a preliminary analysis of vertical velocity and VHF reconstructed using SWOT observations of SSH versus conventional altimetry (DUACS). Appendix B shows how the 2D SWOT SSH field was created from consecutive swaths, and more detailed analysis and validation will be done in a subsequent study. As a first test of the effective sQG reconstruction with SWOT data, we have performed a simple spline interpolation to combine 5 consecutive and neighboring SWOT swaths. These are preliminary beta pre-validated SWOT L3 data (v0.3 PIBO) available from the 21-day science phase of SWOT in October 2023 (see Appendix B and Figure B1). We note that these early SWOT data still need to be validated, especially to understand the signal and noise in the new scales <150 km in wavelength. Wavenumber spectral analyses of SWOT SSH performed along the swaths in this region indicate a consistent spectral energy cascade down to 30–40 km in wavelength, before a second slope is apparent due to noise or internal gravity waves (Vergara et al., 2024). This is consistent with the scales of sQG-observable dynamics from the COAS model (highest spectral coherence for velocity between 30 and 70 km), which is encouraging for applying this sQG reconstruction with SWOT data. The gridded conventional altimetry (DUACS) field used for the sQG is interpolated on the same grid as SWOT. Subsequently, a lowpass filter at 40 km is applied to remove some interpolation residuals that were visible at small scales. For more information about the DUACS product, please refer to (Ballarotta et al., 2019; Taburet et al., 2019). In the case of SWOT and DUACS, the VHF's are computed with the real ARMOR 3D data set (see Section 3.3.1) for the same period and region of the SWOT and DUACS data.

One concern is whether residual measurement noise or ageostrophic high-frequency supertidal signals in the SSH data could be projected vertically by the sQG reconstruction. First, Figure 4 showed that residual high-frequency signals in the wavenumber-frequency spectra from the hourly sQG w were greatly reduced compared to the full COAS model's high-frequency signals. Second, in comparison to the COAS model, SWOT SSH data is corrected for tides and phase-locked internal tides and should have a significantly reduced high-frequency signal. Still, some high-frequency signals and measurement errors may remain. To analyze how this affects the sQG reconstruction, we show the COAS and SWOT joint vorticity-strain probability distribution (JPDF) for the surface velocity fields for a one hourly snapshot in October (see Figure 10). Significant skewness for strain = $\pm\zeta$ is a characteristic of submesoscale fronts. For this model/SWOT snapshot in October, neither COAS nor SWOT present a dominance of points in these regions. The full model velocity and geostrophic fields show a small tail along the cyclonic vorticity axis, which is also evident for SWOT but less energetic. In the case of SWOT, the overall distribution of points is quite similar to the hourly model snapshots. Even if there are high-frequency or noisy residuals remaining in the data, these are not dominant and do not substantially affect the vorticity and strain. This gives us confidence that, at least in this energetic region, these high-frequency or noisy residuals should not highly impact the vertical velocities.

The first test case of applying effective sQG to these SWOT 2D SSH data is shown in Figure 11, compared to the reconstruction based on standard 2D SSH fields from DUACS/Copernicus. These preliminary results indicate that the spatial patterns of reconstructed SWOT w are similar to those derived from the smoother DUACS/Copernicus maps, but with more small-scale structures, even compared to the model sQG reconstruction in Figure 5. Figure 11e shows the vertical profile of the rms of the reconstructed w fields from SWOT and DUACS, and Figure 11f shows similar fields for the VHF. As suggested by the 2D maps, the SWOT reconstructed fields have 50% more rms variability than the smoother DUACS/Copernicus maps.

However, are these small energetic w structures in the SWOT reconstruction realistic or projected noise? To investigate the effect of having additional spatial resolution in the SWOT fields compared to the DUACS/Copernicus fields, we used the sQG reconstructed fields from the COAS SSH field filtered at 20 km (as in Figure 5) to mimic the SWOT resolution, and filtered at 100 km to mimic the resolution of the gridded altimetry maps from DUACS/Copernicus. The rms variability of the filtered model results are very similar to the sQG

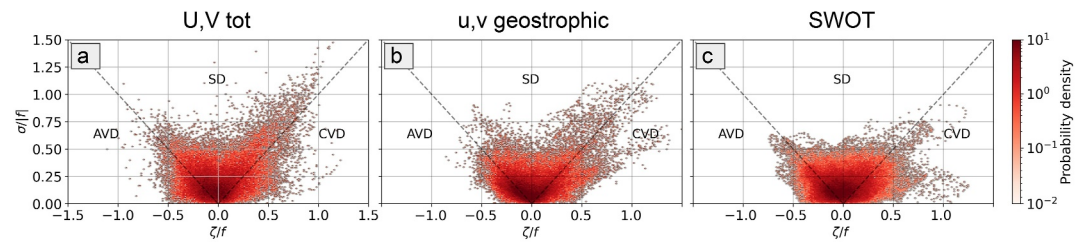


Figure 10. Joint probability distribution of normalized vorticity versus normalized strain rate computed at the surface with the (a) total COAS velocity U and V fields lowpass filtered at 20 km, (b) COAS geostrophic velocities from the SSH lowpass filtered at 20 km, (c) the SWOT SSH 2D interpolated field lowpass filtered at 20 km. Dashed lines in (a)–(c) represent where strain = $|\zeta|$. These lines set boundaries between (SD) strain dominated, (AVD) anticyclonic vorticity dominated, (CVD) cyclonic vorticity dominated regions. COAS figures refer to one hourly snapshot at 00UTC on October 25th.

reconstruction from the SWOT or DUACS data. This suggests that its mainly the increased resolution of the 2D small-scale features in the SWOT SSH that improve the w and VHF reconstruction by adding small wavelengths (up to the sQG capabilities), doubling the rms variability compared to the reconstruction with current altimetry maps. These results show a good statistical comparison in the reconstructed SWOT and COAS reconstructed w and VHF fields, and having comparable SSH spectra (see Figure B1d). SWOT may still have some residual noise effects, but we are achieving similar performance to the reconstruction based on the idealized coupled simulation.

6. Discussion

This work aims to investigate the use of effective sQG for reconstructing vertical velocities and vertical heat fluxes in an energetic region south of Tasmania. Strong mesoscale strain and relative vorticity in this region make it a hotspot for the generation of submesoscale fronts, leading to intense vertical velocities and enhanced vertical fluxes of heat and other tracers. Given the availability of 5 days of data in two contrasting times of the year (March and October), the aim is to demonstrate what physical structures the effective sQG is able to reconstruct at these specific times without focusing on the full seasonal cycle.

For the effective sQG reconstruction, we need to tune two parameters. We use a constant value for the vertical stratification parameter and optimize it iteratively against the relative vorticity reconstruction below the mixed layer, finding a small difference between March and October. A different choice could be to take climatological

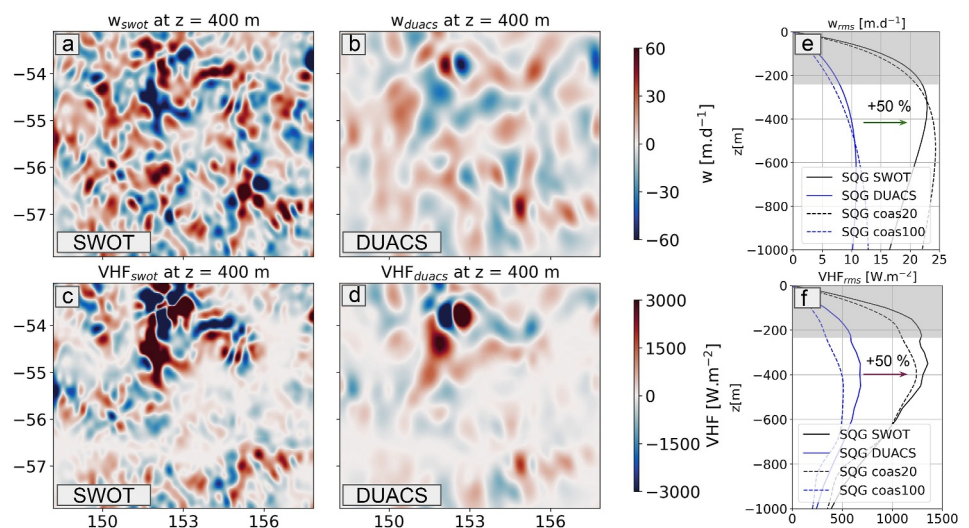


Figure 11. (a and b) sQG w and (c and d) VHF computed with the sQG w and the ready ARMOR 3D product for the week of the 24th of October 2023 from SWOT SSH data (a–c) and from the DUACS SSH (b–d). Rms of (e) w and (f) VHF for the SWOT and DUACS fields (black and blue solid lines, respectively). Rms from the COAS field lowpass filtered at 20 km and lowpass filtered at 100 km are added (black and blue dashed lines, respectively) for comparison. The gray shading is the average mixed layer depth in October.

values for the vertical stratification or to compute an average value from existing ARGO floats. Indeed, for a longer time series over multiple years/seasons, this would need to be tested to set a seasonally varying vertical stratification parameter. For the parameter c , the tuning is performed on the 2D physical fields. In this particular region, non-QG dynamics in the model can impact the stability of this parametrization. More analysis is needed in less energetic regions to test the robustness of this methodology.

After parametrizing the sQG coefficients, this study shows that w in this region can be reconstructed in the first 1,000 m of the water column with a spatial correlation of 0.6 against the daily averaged w fields from the full COAS model. The main result of this study is that the reconstructed field captures most of the variance along the water column (fully at the surface, gradually decreasing to 70% at 1,000 m depth over the full domain), at frequencies $< f$ where sQG is valid. The small-scale reconstructed structures have the highest spectral coherence at scales between 20 and 70 km, with coherent scales increasing from below the mixed layer to larger scales at depth. Here, we interpret our effective sQG results only below the mixed layer since we find, as in previous studies (Klein et al., 2009; Qiu et al., 2020), that the sQG methodology cannot fully represent the mixed layer dynamics. This is, in fact, a first estimation of the feasibility of using the effective sQG in this energetic region. It could be expanded to improve the reconstruction both at depth and within the mixed layer, using improved theories.

Within the mixed layer, other parametrizations accounting for improved dynamics representation have been proposed in the literature. Ponte et al. (2013) demonstrate the impact of wind-driven mixed layer dynamics on vertical velocities in the case of small wind-driven velocities compared to those associated with eddies and an Ekman number not small. Callies et al. (2016) highlight the importance of mixed-layer instabilities compared to mesoscale-driven surface frontogenesis. Chavanne and Klein (2016) include diabatic vertical velocities in the surface layer based on thermal wind balance restoration after perturbations due to turbulent vertical mixing of momentum and buoyancy. These could also be explored in this Southern Ocean region in the future.

Below the mixed layer, the major components contributing to the 30% missing rms in the sQG reconstruction are the depth-intensified vertical velocities, the smaller 20–30 km barotropic structures present on the full water column, and the small-scale wave structures at depth highlighted in Figure 3. The analysis over 5 days in two seasons does not allow a quantitative analysis of the specific dynamics that these features represent. However, the strong deep vertical velocities could be due to the interaction of the flow with the bathymetry at the level of the Southeast Indian ridge. A barotropic component of the flow downstream could cause the intensification of the vertical velocities, which the effective sQG would not reconstruct. In addition to barotropic structures, subsurface intensified eddies, as explained in Section 3.2, are not directly reconstructed by the effective sQG even if they present a SSH signature. Assassi et al. (2016) have identified two indexes that define the type of the eddy (surface, subsurface) based on SSH and surface density/SST information, that could be used to gain prior knowledge on the type of surface or sub-surface structures that may be reconstructed by sQG in a region, given a field of SSH and SST. An alternative approach to capture more of the depth-intensified w could be to use the extended interior and surface quasigeostrophic (isQG) theory from Wang et al. (2013) and Liu et al. (2019), which yields good results in other regions (e.g., South Atlantic Ocean). Miracca-Lage et al. (2022) found a strong dependency of the results on the mixed layer depth and improved results with the isQG compared to the effective sQG. Nevertheless, the 30% degradation of the reconstructed results at depth remains an issue.

To estimate vertical heat fluxes, having temperature anomalies at the same resolution as the w field is still challenging. In particular, reconstructing the temperature anomalies with sQG density anomalies presents some limitations in this region of distinct dynamics and vertical water mass layers north and south of the polar front. Specifically, sQG density anomalies do not capture the temperature anomaly inversions along the water column and coherently project the SSH gradients at depth, changing the real distribution of water masses, especially south of the polar front. The sQG reconstruction of temperature anomalies in the domain also requires a specific linear regression between density and temperature tuned to the area for each season. This is a limiting requirement for using this methodology more widely to compute vertical heat fluxes. To overcome this limitation, we have tested using a pseudo-gridded temperature product with the same resolution in our region as the operational ARMOR 3D product (Guinehut et al., 2012), which smooths out the small scales (< 150 km) compared to the sQG reconstruction, but is spatially better correlated to the reference temperature from the model and captures the mixed layer variability. The spatial scales represented by ARMOR 3D are limited by the present generation of 2D gridded altimetry maps. In the future, we can expect higher-resolution altimetry maps including SWOT, that can be used to stir and reconstruct the ARMOR 3D temperature and salinity fields, and thus have similar high

resolution of 2D surface SSH and 3D T/S fields. Other methodologies exist for reconstructing temperature at depth from SSH, such as the gravest empirical mode (GEM) used by Swart et al. (2010) south of Africa or Meunier et al. (2022) in the Gulf of Mexico, or new machine learning methodologies (Champenois & Sapsis, 2024), which could also be explored in future studies.

VHF are computed for both temperature data sets using the same sQG w fields. Results indicate that the vertical velocity has a dominant role in the reconstruction. In fact, we obtain comparable spatial correlations and rms with the two methods below the mixed layer, even though the two temperature products have quite different metrics, especially in terms of spatial correlation. Improving the w correlation to more than 0.6 would yield to better results for the VHF computed with the pseudo-ARMOR temperature product. The pseudo-ARMOR product offers improved results within the mixed layer in terms of rms. The downside of using such product is that the 150 km resolution hides small mesoscale and submesoscale dynamics. Zhang et al. (2023) found that the submesoscales (<40 km) amplify the VHF via the inverse cascade, which explains the underestimation of the VHF in particular with the pseudo-ARMOR temperature. We have examined two contrasting seasonal examples for this first demonstration of VHF derived from SSH data alone. Although March and October show comparable results, the limited data available (5 days for each month) do not allow for a thorough seasonal comparison.

The potential of this effective sQG reconstruction in the Southern Ocean around 50°S is that every 5 days during the 3-year of the SWOT science mission, it may be possible to estimate a high-resolution 2D map of the vertical velocities and vertical heat fluxes for frequencies $<f$ and from data alone. We have shown that SWOT maps interpolated over 5 days allow a vertical reconstruction with double the rms both in w and VHF compared to current altimetry. We are cautious that there might still be some residual errors or high-frequency information in the SSH data. However, even with the full tide and internal tide fields included in the COAS model, the sQG reconstruction applied to the model SSH shows a greatly reduced effect on the interior w . Moreover, if there are any residual errors in the SWOT data, we showed that this does not give any major bias in the strain and relative vorticity fields compared to the model with no measurement error. Further investigation is needed to quantify the influence of these high-frequency and noise residuals, but we are confident that these sQG reconstructions from the SWOT SSH fields are comparable to the idealistic simulated field in this energetic region. The next step is to carefully validate the SWOT data against in situ ground-truth data of 3D velocities and temperature at depth, and this will be the subject of an upcoming study. This methodology could then be extended to larger domains in the energetic Southern Ocean to evaluate the vertical exchanges between the surface and the ocean interior on a regular basis.

Our study has demonstrated that effective sQG can reconstruct up to 70% of the modeled vertical velocities larger than 30–40 km in wavelength in this region and 60%–70% of the vertical heat fluxes at these scales. There are limitations in the sQG vertical projection from the surface to depth, which cannot capture the vertical velocities generated at depth downstream of the Southeast East Indian Ridge and cannot capture the small-scale w (< 40 km), nor from frequencies $>f$ (internal waves, inertial oscillations, etc). Another limitation is that fast-evolving structures would still be missed because of the SWOT 21-day coverage (see Appendix B for SWOT coverage over the region). Indeed, in our simple interpolation, we take the central date as a reference and assume that the observed structures in neighboring passes offset by 1-day are static over each 5-day period. This assumption is similar to that used with most ship-borne campaigns in reconstructing the 3D field over many days. CNES and Collecte Localisation Satellites (CLS) are working on a higher-resolution 2D multi-altimeter SSH operational product like DUACS/Copernicus that will include SWOT. This product will include more small scales compared to the current Copernicus operational product, but any mapping procedure will still smooth some of the small scales observed within the swaths. Ideally, some regional high-resolution mapping may be developed in the future to reduce this smoothing. These improved future operational 2D gridded SSH data maps that include SWOT data will also help improve derived products like ARMOR 3D due to, for example, better localization of eddies. This will increase the spatial resolution and potentially avoid the temperature and VHF underestimation of the vertical water column.

Appendix A: sQG Reconstruction of Temperature Anomalies

Temperature anomalies can be reconstructed with only altimetry data, using sQG. Two preliminary analyses have been carried out to ensure that this anomaly can be retrieved from the sQG density anomalies.

A1. Stability at the Base of the Mixed Layer

The ocean density is a function of the 3D structure of the water temperature, salinity and pressure and depends strongly on the temperature and salinity structure. The Brunt-Vařsala frequency coefficient N , a function of the density gradient, dictates the stability of the water column. It is defined as

$$N^2 = \frac{g}{\rho} \frac{\partial \rho}{\partial z} \quad (\text{A1})$$

where g is the gravitational constant, ρ is the density and z is the water depth. The necessary condition for water column stability is a positive N . This stability can be split into the contribution of the thermal and haline parts

$$\frac{1}{\rho} \frac{\partial \rho}{\partial z} = -\alpha \frac{\partial T}{\partial z} + \beta \frac{\partial S}{\partial z} \quad (\text{A2})$$

where $\alpha = \frac{1}{\rho} \frac{\partial \rho}{\partial T}$ and $\beta = \frac{1}{\rho} \frac{\partial \rho}{\partial S}$. The two terms representing the role of the thermal and haline stratification on the stability at the base of the mixed layer are the thermal stability $N_T = -g\alpha \frac{\partial T}{\partial z}$ and the haline stability $N_S = g\beta \frac{\partial S}{\partial z}$. Where thermal stability dominates, the density gradient is driven by the temperature, so we can suppose that the temperature measurements in the region are sufficient to retrieve the density. The opposite is true when the haline stability dominates. We first verified that in this polar front region, the thermal stability dominated over the haline stability at all levels (this is not the case in the sea-ice zone further south).

Then, by building scatter plots between the density and temperature anomalies, we can investigate the relationship between those two variables as a function of depth and season.

A2. Linear Correlation Between Density and Temperature Anomalies

The linear regression is built for each vertical layer from the COAS density and temperature spatial anomalies (taken with respect to the mean of the 2D detrended spatial field). Figure A1 shows two examples of the scatter and linear regression below the mixed layer, where the regression improves with depth. Figure A1c provides the values of the linear regression slope at each depth. Below the mixed layer, these values are similar in March and October and are consistent during the 5 days. The intercept value is close to zero in all cases. At 251 m, the temperature values still present some extreme values that are overestimated or underestimated by the linear regression. At 613 m, the anomalies are more concentrated around zero (see the distribution of the variables), the scatter itself presents a more linear shape, and there are fewer points with extreme values. The density and temperature have an increasingly linear relation with depth, with fewer points of temperature extremes departing

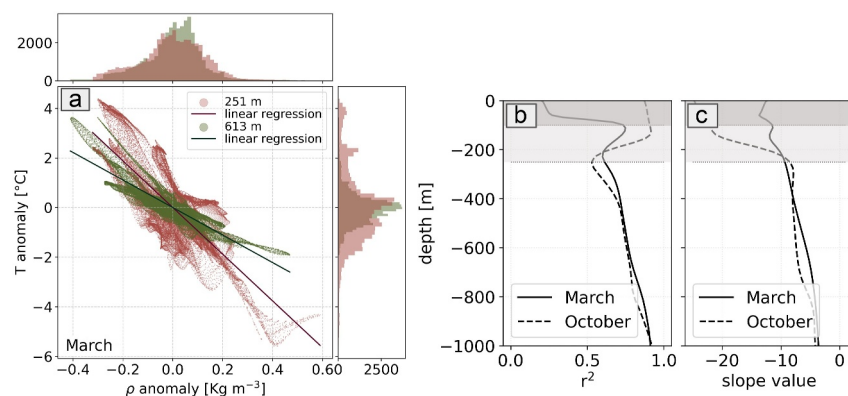


Figure A1. (a) Scatter plot between density anomalies and temperature anomalies for COAS at 251 and 613 m, with the respective linear regression used to reconstruct the temperature anomalies. The distribution of each variable is also shown in the lateral plots. Example for March. (b) Significance coefficient (r^2) of the linear regression and (c) values of the linear regression at each depth for March and October. The gray shading corresponds to the average mixed layer (ML) in the region for the 5 days between March 25th and 29th (dark gray), and between October 25th and 29th (light gray).

from it. This is shown in Figure A1b, where the significance coefficient r^2 is close to 0.5 at the bottom of the ML for both seasons, gradually increasing up to 0.9 at depth. The p-value of all regressions is below 0.05, a threshold usually taken to test the null hypothesis (not shown). This indicates the statistical significance of the regression. Once the fine-resolution density anomalies are reconstructed with sQG, the temperature anomalies are deduced by implementing the linear regression mentioned above for each depth.

For this study, we have used the COAS model with full temperature/density field sampling and derived these statistical linear correlations in our region, at each model vertical level, and in contrasting seasons. For a wider application based on observations only, these linear correlations would need to be derived globally from Argo/hydrography profiles, for example, and with monthly variations.

Appendix B: SWOT Orbit and Coverage in the Study Area

The Sea Level Anomaly (SLA) swaths used to build the 2D field for applying the sQG methodology to the SWOT data are created using the v0.3 (PIB0) beta pre-validated L3 product. This product has SLA filtered with the U-net algorithm from Tréboutte et al. (2023) to which the Gomez filter from Gómez-Navarro et al. (2020) is subsequently applied. These data are published by AVISO (<https://doi.org/10.24400/527896/A01-2023.017>) (AVISO/DUACS, 2023). During the 3-year science phase, SWOT covers the region of interest for this study completely in 21-day. However, due to the orbit coverage, there are four windows in which the satellite observes the region during five consecutive days, with swaths laid down in two sets of alternate ascending and descending passes that fully cover the area (see Figure B1a). These 5-day neighboring swaths are then used to create a 2D high-resolution SSH map over 600×600 km, by interpolating neighboring swaths using a spline interpolation (see Figure B1b). This field is then filtered at 20 km to imitate the sQG processing described in the main text, and to reduce the SWOT noise, for example, from the interpolation across gaps and from residual waves, etc. The corresponding DUACS 2D field centered on the same date is illustrated in Figure B1c for comparison.

The SSH wavelength spectra of the 2D interpolated SWOT field, the DUACS field and the full COAS simulation are represented in Figure B1d. The three spectra match at large scales, down to ~ 100 km. Below, DUACS presents

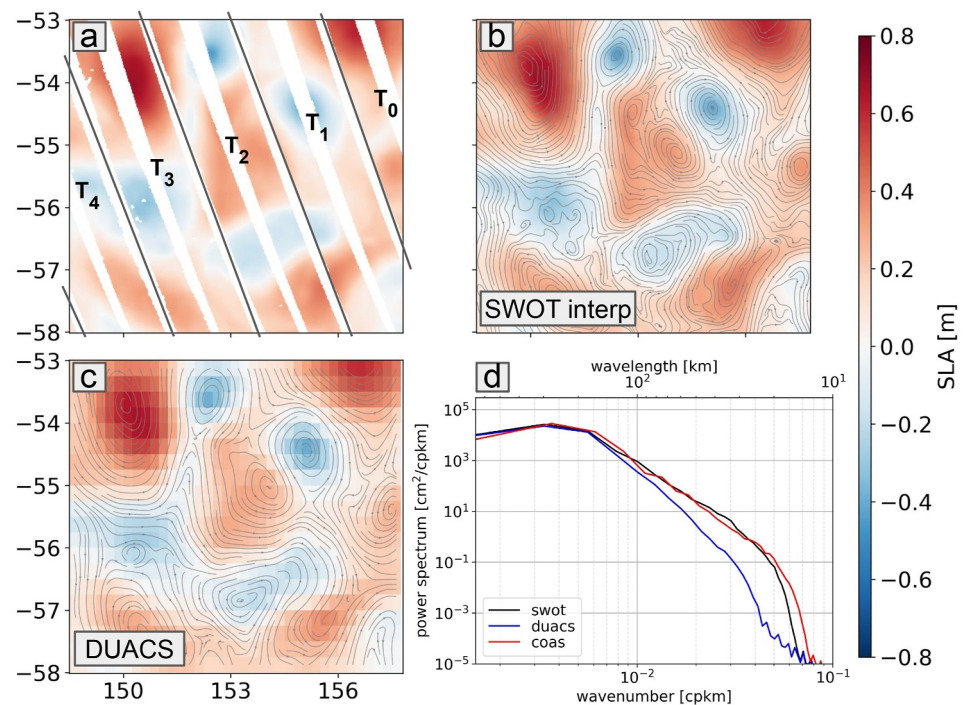


Figure B1. (a) L3 SWOT Sea Level Anomaly over 5 days in October, (b) spline interpolation of the previous field, (c) DUACS SSH centered in the central day of SWOT observations, (d) SSH spectra of the 2D SWOT field, the DUACS field on the same region and period, and of COAS in the same area and season.

lower energy than COAS and SWOT, and SWOT has slightly higher energy than COAS from 25 to 40 km. Different processes could cause this. On one hand, SWOT data and COAS have a better representation of small scales than the DUACS product, leading to improved vertical dynamics in the region. On the other hand, this part of the spectrum could also include SWOT errors from new altimetric corrections at 2 km scales and from residual instrumental noise.

Data Availability Statement

The code developed for the SSH-based diagnostics was created using Python 3.9 and is available upon request. The Jet Propulsion Laboratory has provided the COAS simulation outputs. The SWOT_L3_SSH product, derived from the L2 SWOT KaRIn Low rate ocean data products (NASA/JPL and CNES), is produced and made freely available by AVISO and DUACS teams as part of the DESMOS Science Team project. AVISO/DUACS (2023) SWOT Level-3 SSH Basic (v0.3 PIB0) [Dataset]. CNES. <https://doi.org/10.24400/527896/A01-2023.017>. The ARMOR 3D data are open source and available at <https://doi.org/10.48670/moi-00052>.

Acknowledgments

Elisa Carli was supported by the Centre National d'Études Spatiales (CNES) and Collecte Localisation Satellites (CLS) with a co-funded research grant to conduct her PhD. This work was financed through the CNES SWOT TOSCA project and partially supported through the grant EUR TESS No. ANR-18-EURE-0018 in the framework of the Programme des Investissements d'Avenir. We thank Patrice Klein, Lionel Renault, and Jonathan Gula for their precious comments on the manuscript. We thank Tredren Tranchant for insightful discussion on SWOT data interpolation.

References

- Allen, J. T., Smeed, D. A., Nurser, A. J. G., Zhang, J. W., & Rixen, M. (2001). Diagnosis of vertical velocities with the QG omega equation: An examination of the errors due to sampling strategy. *Deep Sea Research Part I: Oceanographic Research Papers*, 48(2), 315–346. [https://doi.org/10.1016/S0967-0637\(00\)00035-2](https://doi.org/10.1016/S0967-0637(00)00035-2)
- Arbic, B. K., Alford, M. H., Ansong, J. K., Buijsman, M. C., Ciotti, R. B., Farrar, J. T., et al. (2018). Primer on global internal tide and internal gravity wave continuum modeling in HYCOM and MITgcm. *New Frontiers in Operational Oceanography*, 307–392. Retrieved from <https://diginole.lib.fsu.edu/islandora/object/fsu%3A602131/>
- Assassi, C., Morel, Y., Vandermeersch, F., Chaigneau, A., Pegliasco, C., Morrow, R., et al. (2016). An index to distinguish surface- and subsurface-intensified vortices from surface observations. *Journal of Physical Oceanography*, 46(8), 2529–2552. <https://doi.org/10.1175/JPO-D-15-0122.1>
- AVISO/DUACS. (2023). SWOT Level-3 KaRIn Low Rate SSH Basic [Dataset]. CNES. <https://doi.org/10.24400/527896/A01-2023.017>
- Ballarotta, M., Ubelmann, C., Pujol, M.-L., Taburet, G., Fournier, F., Legeais, J.-F., et al. (2019). On the resolutions of ocean altimetry maps. *Ocean Science*, 15(4), 1091–1109. <https://doi.org/10.5194/os-15-1091-2019>
- Barceló-Llull, B., Mason, E., Capet, A., & Pascual, A. (2016). Impact of vertical and horizontal advection on nutrient distribution in the southeast Pacific. *Ocean Science*, 12(4), 1003–1011. <https://doi.org/10.5194/os-12-1003-2016>
- Barceló-Llull, B., Pascual, A., Mason, E., & Mulet, S. (2018). Comparing a multivariate global ocean state estimate with high-resolution in situ data: An anticyclonic intrathermocline eddy near the canary Islands. *Frontiers in Marine Science*, 5. <https://doi.org/10.3389/fmars.2018.00066>
- Boccaletti, G., Ferrari, R., Adcroft, A., Ferreira, D., & Marshall, J. (2005). The vertical structure of ocean heat transport. *Geophysical Research Letters*, 32(10), L10603. <https://doi.org/10.1029/2005GL022474>
- Brannigan, L. (2016). Intense submesoscale upwelling in anticyclonic eddies. *Geophysical Research Letters*, 43(7), 3360–3369. <https://doi.org/10.1002/2016GL067926>
- Callies, J., Ferrari, R., Klymak, J. M., & Gula, J. (2015). Seasonality in submesoscale turbulence. *Nature Communications*, 6(1), 6862. <https://doi.org/10.1038/ncomms7862>
- Callies, J., Flierl, G., Ferrari, R., & Fox-Kemper, B. (2016). The role of mixed-layer instabilities in submesoscale turbulence. *Journal of Fluid Mechanics*, 788, 5–41. <https://doi.org/10.1017/jfm.2015.700>
- Champanois, B., & Sapsis, T. (2024). Machine learning framework for the real-time reconstruction of regional 4D ocean temperature fields from historical reanalysis data and real-time satellite and buoy surface measurements. *Physica D: Nonlinear Phenomena*, 459, 134026. <https://doi.org/10.1016/j.physd.2023.134026>
- Charney, J. G. (1971). Geostrophic turbulence. *Journal of the Atmospheric Sciences*, 28(6), 1087–1095. [https://doi.org/10.1175/1520-0469\(1971\)028<1087:GT>2.0.CO;2](https://doi.org/10.1175/1520-0469(1971)028<1087:GT>2.0.CO;2)
- Chavanne, C. P., & Klein, P. (2016). Quasigeostrophic diagnosis of mixed layer dynamics embedded in a mesoscale turbulent field. *Journal of Physical Oceanography*, 46(1), 275–287. <https://doi.org/10.1175/JPO-D-14-0178.1>
- Cyriac, A., Meyer, A., Phillips, H. E., & Bindoff, N. L. (2023). Observations of internal wave interactions in a Southern Ocean standing meander. *Journal of Physical Oceanography*, 53(8), 1997–2011. <https://doi.org/10.1175/JPO-D-22-0157.1>
- de Boyer Montégut, C., Madec, G., Fischer, A. S., Lazar, A., & Iudicone, D. (2004). Mixed layer depth over the global ocean: An examination of profile data and a profile-based climatology. *Journal of Geophysical Research*, 109(C12), C12003. <https://doi.org/10.1029/2004JC002378>
- Dibarboure, G., Anadon, C., Briol, F., Cadier, E., Chevrier, R., Delepouille, A., et al. (2024). Blending 2D topography images from SWOT into the altimeter constellation with the Level-3 multi-mission DUACS system. <https://doi.org/10.5194/egusphere-2024-1501>
- Dibarboure, G., Ubelmann, C., Faugere, Y., Delepouille, A., Briol, F., Chevrier, R., et al. (2023). *SWOT Level-3 overview algorithms and examples*. Toulouse.
- Dong, S., Sprintall, J., & Gille, S. T. (2006). Location of the Antarctic polar front from AMSR-E satellite sea surface temperature measurements. *Journal of Physical Oceanography*, 36(11), 2075–2089. <https://doi.org/10.1175/JPO2973>
- d'Ovidio, F., Pascual, A., Wang, J., Doglioli, A. M., Jing, Z., Moreau, S., et al. (2019). Frontiers in fine-scale in situ studies: Opportunities during the SWOT fast sampling phase. *Frontiers in Marine Science*, 6, 168. <https://doi.org/10.3389/fmars.2019.00168>
- Duchon, C. E. (1979). Lanczos filtering in one and two dimensions. *Journal of Applied Meteorology and Climatology*, 18(8), 1016–1022. [https://doi.org/10.1175/1520-0450\(1979\)018<1016:LFIOTAT>2.0.CO;2](https://doi.org/10.1175/1520-0450(1979)018<1016:LFIOTAT>2.0.CO;2)
- Foppert, A., Donohue, K. A., Watts, D. R., & Tracey, K. L. (2017). Eddy heat flux across the Antarctic circumpolar current estimated from sea surface height standard deviation. *Journal of Geophysical Research: Oceans*, 122(8), 6947–6964. <https://doi.org/10.1002/2017JC012837>
- Fox-Kemper, B., Ferrari, R., & Hallberg, R. (2008). Parameterization of mixed layer eddies. Part I: Theory and diagnosis. *Journal of Physical Oceanography*, 38(6), 1145–1165. <https://doi.org/10.1175/2007JPO3792>

- Franks, P. J. S., Wroblewski, J. S., & Flierl, G. R. (1986). Prediction of phytoplankton growth in response to the frictional decay of a warm-core ring. *Journal of Geophysical Research*, *91*(C6), 7603–7610. <https://doi.org/10.1029/JC091iC06p07603>
- Frenger, I., Münnich, M., Gruber, N., & Knutti, R. (2015). Southern Ocean eddy phenomenology. *Journal of Geophysical Research: Oceans*, *120*(11), 7413–7449. <https://doi.org/10.1002/2015JC011047>
- Fu, L., Pavelsky, T., Cretaux, J., Morrow, R., Farrar, J., Vaze, P., et al. (2024). The surface water and ocean topography mission: A breakthrough in radar remote sensing of the ocean and land surface water. *Geophysical Research Letters*, *51*(4), e2023GL107652. <https://doi.org/10.1029/2023GL107652>
- Gómez-Navarro, L., Cosme, E., Sommer, J. L., Papadakis, N., & Pascual, A. (2020). Development of an image de-noising method in preparation for the surface water and ocean topography satellite mission. *Remote Sensing*, *12*(4), 734. <https://doi.org/10.3390/rs12040734>
- Griffies, S. M., Winton, M., Anderson, W. G., Benson, R., Delworth, T. L., Dufour, C. O., et al. (2015). Impacts on ocean heat from transient mesoscale eddies in a hierarchy of climate models. *Journal of Climate*, *28*(3), 952–977. <https://doi.org/10.1175/JCLI-D-14-00353.1>
- Guinehut, S., Dhomp, A.-L., Larnicol, G., & Le Traon, P.-Y. (2012). High resolution 3-D temperature and salinity fields derived from in situ and satellite observations. *Ocean Science*, *8*(5), 845–857. <https://doi.org/10.5194/os-8-845-2012>
- Hogg, A. M. C., Meredith, M. P., Blundell, J. R., & Wilson, C. (2008). Eddy heat flux in the Southern Ocean: Response to variable wind forcing. *Journal of Climate*, *21*(4), 608–620. <https://doi.org/10.1175/2007JCLI1925.1>
- Hoskins, B. J., Draghici, I., & Davies, H. C. (1978). A new look at the w-equation. *Quarterly Journal of the Royal Meteorological Society*, *104*(439), 31–38. <https://doi.org/10.1002/qj.49710443903>
- Hua, B., & Klein, P. (1998). An exact criterion for the stirring properties of nearly two-dimensional turbulence. *Physica D: Nonlinear Phenomena*, *113*(1), 98–110. [https://doi.org/10.1016/S0167-2789\(97\)00143-7](https://doi.org/10.1016/S0167-2789(97)00143-7)
- Hughes, C. W., Jones, M. S., & Carnochan, S. (1998). Use of transient features to identify eastward currents in the Southern Ocean. *Journal of Geophysical Research*, *103*(C2), 2929–2943. <https://doi.org/10.1029/97JC02442>
- Intergovernmental Panel On Climate Change (IPCC). (2022). *The ocean and cryosphere in a changing climate: Special report of the intergovernmental panel on climate change* (1st ed.). Cambridge University Press. <https://doi.org/10.1017/9781009157964>
- Jakes, M. I., Phillips, H. E., Foppert, A., Cyriac, A., Bindoff, N. L., Rintoul, S. R., & Thompson, A. F. (2024). Observational evidence of cold filamentary intensification in an energetic meander of the Antarctic circumpolar current. *Journal of Physical Oceanography*, *54*(3), 717–740. <https://doi.org/10.1175/JPO-D-23-0085.1>
- Klein, P., Hua, B. L., Lapeyre, G., Capet, X., Gentil, S. L., & Sasaki, H. (2008). Upper ocean turbulence from high-resolution 3D simulations. *Journal of Physical Oceanography*, *38*(8), 1748–1763. <https://doi.org/10.1175/2007JPO3773>
- Klein, P., Isern-Fontanet, J., Lapeyre, G., Roullet, G., Danioux, E., Chapron, B., et al. (2009). Diagnosis of vertical velocities in the upper ocean from high resolution sea surface height. *Geophysical Research Letters*, *36*(12), L12603. <https://doi.org/10.1029/2009GL038359>
- Klein, P., & Lapeyre, G. (2009). The oceanic vertical pump induced by mesoscale and submesoscale turbulence. *Annual Review of Marine Science*, *1*(1), 351–375. <https://doi.org/10.1146/annurev.marine.010908.163704>
- Lapeyre, G. (2017). Surface quasi-geostrophy. *Fluids*, *2*(1), 7. <https://doi.org/10.3390/fluids2010007>
- Lapeyre, G., & Klein, P. (2006). Dynamics of the upper oceanic layers in terms of surface quasigeostrophy theory. *Journal of Physical Oceanography*, *36*(2), 165–176. <https://doi.org/10.1175/JPO2840>
- Le Sommer, J., d'Ovidio, F., & Madec, G. (2011). Parameterization of subgrid stirring in eddy resolving ocean models. Part 1: Theory and diagnostics. *Ocean Modelling*, *39*(1), 154–169. <https://doi.org/10.1016/j.ocemod.2011.03.007>
- Lévy, M. (2024). Menace sur l'océan. La jaune et la rouge [revue mensuelle de la société amicale des anciens élèves de l'Ecole Polytechnique] (Technical Report No. 791).
- Liu, L., Xue, H., & Sasaki, H. (2019). Reconstructing the ocean interior from high-resolution sea surface information. *Journal of Physical Oceanography*, *49*(12), 3245–3262. <https://doi.org/10.1175/JPO-D-19-0118.1>
- Llort, J., Langlais, C., Matear, R., Moreau, S., Lenton, A., & Strutton, P. G. (2018). Evaluating Southern Ocean carbon eddy-pump from biogeochemical-Argo floats. *Journal of Geophysical Research: Oceans*, *123*(2), 971–984. <https://doi.org/10.1002/2017JC012861>
- Mahadevan, A., & Archer, D. (2000). Modeling the impact of fronts and mesoscale circulation on the nutrient supply and biogeochemistry of the upper ocean. *Journal of Geophysical Research*, *105*(C1), 1209–1225. <https://doi.org/10.1029/1999JC900216>
- Marshall, J., Shuckburgh, E., Jones, H., & Hill, C. (2006). Estimates and implications of surface eddy diffusivity in the Southern Ocean derived from tracer transport. *Journal of Physical Oceanography*, *36*(9), 1806–1821. <https://doi.org/10.1175/JPO2949>
- Martin, A. P., & Richards, K. (2001). Mechanisms for vertical nutrient transport within North Atlantic mesoscale eddy. *Deep-Sea Research Part II-Topical Studies in Oceanography*, *48*(4–5), 757–773. [https://doi.org/10.1016/S0967-0645\(00\)00096-5](https://doi.org/10.1016/S0967-0645(00)00096-5)
- Martin, A. P., Richards, K. J., Bracco, A., & Provenzale, A. (2002). Patchy productivity in the open ocean. *Global Biogeochemical Cycles*, *16*(2), 9–1–9–9. <https://doi.org/10.1029/2001GB001449>
- Martin, A. P., Richards, K. J., Law, C. S., & Liddicoat, M. (2001). Horizontal dispersion within an anticyclonic mesoscale eddy. *Deep Sea Research Part II: Topical Studies in Oceanography*, *48*(4), 739–755. [https://doi.org/10.1016/S0967-0645\(00\)00095-3](https://doi.org/10.1016/S0967-0645(00)00095-3)
- Martínez Moreno, J., Hogg, A., England, M., Constantinou, N., Kiss, A., & Morrison, A. (2020). Global changes in oceanic mesoscale currents over the satellite altimetry record. <https://doi.org/10.21203/rs.3.rs-88932/v1>
- Mason, E., Pascual, A., Gaube, P., Ruiz, S., Pelegrí, J. L., & Delepuille, A. (2017). Subregional characterization of mesoscale eddies across the Brazil-Malvinas Confluence. *Journal of Geophysical Research: Oceans*, *122*(4), 3329–3357. <https://doi.org/10.1002/2016JC012611>
- McGillicuddy, D. J., Anderson, L. A., Bates, N. R., Bibby, T., Buesseler, K. O., Carlson, C. A., et al. (2007). Eddy/wind interactions stimulate extraordinary mid-ocean plankton blooms. *Science*, *316*(5827), 1021–1026. <https://doi.org/10.1126/science.1136256>
- McWilliams, J. C. (1989). Statistical properties of decaying geostrophic turbulence. *Journal of Fluid Mechanics*, *198*(-1), 199–230. <https://doi.org/10.1017/S00222112089000108>
- Meijer, J. J., Phillips, H. E., Bindoff, N. L., Rintoul, S. R., & Foppert, A. (2022). Dynamics of a standing meander of the subantarctic front diagnosed from satellite altimetry and along-stream anomalies of temperature and salinity. *Journal of Physical Oceanography*, *52*(6), 1073–1089. <https://doi.org/10.1175/JPO-D-21-0049.1>
- Meunier, T., Pérez-Brunius, P., & Bower, A. (2022). Reconstructing the three-dimensional structure of loop current rings from satellite altimetry and in situ data using the gravest empirical modes method. *Remote Sensing*, *14*(17), 4174. <https://doi.org/10.3390/rs14174174>
- Miracca-Lage, M., González-Haro, C., Napolitano, D. C., Isern-Fontanet, J., & Polito, P. S. (2022). Can the surface quasi-geostrophic (SQG) theory explain upper ocean dynamics in the South Atlantic? *Journal of Geophysical Research: Oceans*, *127*(2), e2021JC018001. <https://doi.org/10.1029/2021JC018001>
- Molod, A., Takacs, L., Suarez, M., & Bacmeister, J. (2015). Development of the GEOS-5 atmospheric general circulation model: Evolution from MERRA to MERRA2. *Geoscientific Model Development*, *8*(5), 1339–1356. <https://doi.org/10.5194/gmd-8-1339-2015>

- Morrow, R., Birol, F., Griffin, D., & Sudre, J. (2004). Divergent pathways of cyclonic and anti-cyclonic ocean eddies. *Geophysical Research Letters*, 31(24), L24311. <https://doi.org/10.1029/2004GL020974>
- Morrow, R., Fu, L.-L., Arduini, F., Benkiran, M., Chapron, B., Cosme, E., et al. (2019). Global observations of fine-scale ocean surface topography with the surface water and ocean topography (SWOT) mission. *Frontiers in Marine Science*, 6. <https://doi.org/10.3389/fmars.2019.00232>
- Mulet, S., Rio, M. H., Mignot, A., Guinehut, S., & Morrow, R. (2012). A new estimate of the global 3D geostrophic ocean circulation based on satellite data and in-situ measurements. *Deep Sea Research Part II: Topical Studies in Oceanography*, 77–80, 70–81. <https://doi.org/10.1016/j.dsr2.2012.04.012>
- Naveira Garabato, A. C., Ferrari, R., & Polzin, K. L. (2011). Eddy stirring in the Southern Ocean. *Journal of Geophysical Research*, 116(C9), C9019. <https://doi.org/10.1029/2010JC006818>
- Nencioli, F., d'Ovidio, F., Doglioli, A. M., & Petrenko, A. A. (2013). In situ estimates of submesoscale horizontal eddy diffusivity across an ocean front. *Journal of Geophysical Research: Oceans*, 118(12), 7066–7080. <https://doi.org/10.1002/2013JC009252>
- Pascual, A., Ruiz, S., Buongiorno Nardelli, B., Guinehut, S., Iudicone, D., & Tintoré, J. (2015). Net primary production in the Gulf Stream sustained by quasi-geostrophic vertical exchanges. *Geophysical Research Letters*, 42(2), 441–449. <https://doi.org/10.1002/2014GL062569>
- Patel, R. S., Llorc, J., Strutton, P. G., Phillips, H. E., Moreau, S., Conde Pardo, P., & Lenton, A. (2020). The biogeochemical structure of Southern Ocean mesoscale eddies. *Journal of Geophysical Research: Oceans*, 125(8), e2020JC016115. <https://doi.org/10.1029/2020JC016115>
- Patel, R. S., Phillips, H. E., Strutton, P. G., Lenton, A., & Llorc, J. (2019). Meridional heat and salt transport across the subantarctic front by cold-core eddies. *Journal of Geophysical Research: Oceans*, 124(2), 981–1004. <https://doi.org/10.1029/2018JC014655>
- Phillips, H. E., & Rintoul, S. R. (2000). Eddy variability and energetics from direct current measurements in the Antarctic circumpolar current South of Australia. *Journal of Physical Oceanography*, 30(12), 3050–3076. [https://doi.org/10.1175/1520-0485\(2000\)030<3050:EVAEFD>2.0.CO;2](https://doi.org/10.1175/1520-0485(2000)030<3050:EVAEFD>2.0.CO;2)
- Ponte, A. L., Klein, P., Capet, X., Traou, P.-Y. L., Chapron, B., & Lherminier, P. (2013). Diagnosing surface mixed layer dynamics from high-resolution satellite observations: Numerical insights. *Journal of Physical Oceanography*, 43(7), 1345–1355. <https://doi.org/10.1175/JPO-D-12-0136.1>
- Qiu, B., Chen, S., Klein, P., Torres, H., Wang, J., Fu, L.-L., & Menemenlis, D. (2020). Reconstructing upper-ocean vertical velocity field from sea surface height in the presence of unbalanced motion. *Journal of Physical Oceanography*, 50(1), 55–79. <https://doi.org/10.1175/JPO-D-19-0172.1>
- Rhein, M., Rintoul, S., Aoki, S., Campos, E., Chambers, D., Feely, R., & Wang, F. (2013). Observations: Ocean. In *Climate change 2013: The physical science basis. Contribution of working group I to the fifth assessment report of the intergovernmental panel on climate change* (pp. 255–315). Fifth Assessment Report of the Intergovernmental Panel on Climate Change.
- Rhines, P. B. (1979). Geostrophic turbulence. *Annual Review of Fluid Mechanics*, 11(1), 401–441. <https://doi.org/10.1146/annurev.fl.11.010179.002153>
- Rintoul, S. R. (2018). The global influence of localized dynamics in the Southern Ocean. *Nature*, 558(7709), 209–218. <https://doi.org/10.1038/s41586-018-0182-3>
- Rocha, C. B., Chereskin, T. K., Gille, S. T., & Menemenlis, D. (2016). Mesoscale to submesoscale wavenumber spectra in Drake Passage. *Journal of Physical Oceanography*, 46(2), 601–620. <https://doi.org/10.1175/JPO-D-15-0087.1>
- Rocha, C. B., Gille, S. T., Chereskin, T. K., & Menemenlis, D. (2016). Seasonality of submesoscale dynamics in the Kuroshio Extension. *Geophysical Research Letters*, 43(21), 11304–11311. <https://doi.org/10.1002/2016GL071349>
- Rudnick, D. L. (1996). Intensive surveys of the Azores Front: 2. Inferring the geostrophic and vertical velocity fields. *Journal of Geophysical Research*, 101(C7), 16291–16303. <https://doi.org/10.1029/96JC01144>
- Sallée, J.-B. (2018). Southern Ocean warming. *Oceanography*, 31(2), 52–62. <https://doi.org/10.5670/oceanog.2018.215>
- Siegelman, L. (2020). Energetic submesoscale dynamics in the ocean interior. *Journal of Physical Oceanography*, 50(3), 727–749. <https://doi.org/10.1175/JPO-D-19-0253.1>
- Siegelman, L., Klein, P., Rivière, P., Thompson, A. F., Torres, H. S., Flexas, M., & Menemenlis, D. (2020). Enhanced upward heat transport at deep submesoscale ocean fronts. *Nature Geoscience*, 13(1), 50–55. <https://doi.org/10.1038/s41561-019-0489-1>
- Strass, V. H. (1992). Chlorophyll patchiness caused by mesoscale upwelling at fronts. *Deep-Sea Research, Part A: Oceanographic Research Papers*, 39(1), 75–96. [https://doi.org/10.1016/0198-0149\(92\)90021-K](https://doi.org/10.1016/0198-0149(92)90021-K)
- Su, Z., Torres, H., Klein, P., Thompson, A. F., Siegelman, L., Wang, J., et al. (2020). High-frequency submesoscale motions enhance the upward vertical heat transport in the global ocean. *Journal of Geophysical Research: Oceans*, 125(9), e2020JC016544. <https://doi.org/10.1029/2020JC016544>
- Su, Z., Wang, J., Klein, P., Thompson, A. F., & Menemenlis, D. (2018). Ocean submesoscales as a key component of the global heat budget. *Nature Communications*, 9(1), 775. <https://doi.org/10.1038/s41467-018-02983-w>
- Sun, B., Liu, C., & Wang, F. (2019). Global meridional eddy heat transport inferred from Argo and altimetry observations. *Scientific Reports*, 9(1), 1–10. <https://doi.org/10.1038/s41598-018-38069-2>
- Swart, S., Speich, S., Anson, I. J., & Lutjeharms, J. R. E. (2010). An altimetry-based gravest empirical mode south of Africa: 1. Development and validation. *Journal of Geophysical Research*, 115(C3), C03002. <https://doi.org/10.1029/2009JC005299>
- Taburet, G., Sanchez-Roman, A., Ballarotta, M., Pujol, M.-I., Legeais, J.-F., Fournier, F., et al. (2019). DUACS DT2018: 25 years of reprocessed sea level altimetry products. *Ocean Science*, 15(5), 1207–1224. <https://doi.org/10.5194/os-15-1207-2019>
- Tamsitt, V., Drake, H. F., Morrison, A. K., Talley, L. D., Dufour, C. O., Gray, A. R., et al. (2017). Spiraling pathways of global deep waters to the surface of the Southern Ocean. *Nature Communications*, 8(1), 172. <https://doi.org/10.1038/s41467-017-00197-0>
- Thomas, L., & Ferrari, R. (2008). Friction, frontogenesis, and the stratification of the surface mixed layer. *Journal of Physical Oceanography*, 38(11), 2501–2518. <https://doi.org/10.1175/2008JPO3797>
- Tintoré, J., Gomis, D., Alonso, S., & Parrilla, G. (1991). Mesoscale dynamics and vertical motion in the Alborán Sea. *Journal of Physical Oceanography*, 21(6), 811–823. [https://doi.org/10.1175/1520-0485\(1991\)021<0811:MDAVMI>2.0.CO;2](https://doi.org/10.1175/1520-0485(1991)021<0811:MDAVMI>2.0.CO;2)
- Torres, H. S., Klein, P., Wang, J., Wineteer, A., Qiu, B., Thompson, A. F., et al. (2022). Wind work at the air-sea interface: A modeling study in anticipation of future space missions. *Geoscientific Model Development*, 15(21), 8041–8058. <https://doi.org/10.5194/gmd-15-8041-2022>
- Tréboutte, A., Carli, E., Ballarotta, M., Carpentier, B., Faugère, Y., & Dibarboure, G. (2023). KaRIn noise reduction using a convolutional neural network for the SWOT ocean products. *Remote Sensing*, 15(8), 2183. <https://doi.org/10.3390/rs15082183>
- Trenberth, E., & Caron, M. (2001). Estimates of meridional atmosphere and ocean heat transports. *Journal of Climate*, 14(16), 3433–3443. [https://doi.org/10.1175/1520-0442\(2001\)014<3433:eomaa0>2.0.co;2](https://doi.org/10.1175/1520-0442(2001)014<3433:eomaa0>2.0.co;2)
- Vergara, O., Morrow, R., Chevrier, R., Dibarboure, G., & Picot, N. (2024). Global Ocean spectral slope rupture evidenced by SWOT 21-day orbit observations. In *EGU General Assembly 2024, Vienna, Austria, 14-19 April 2024*, EGU24-6299. <https://doi.org/10.5194/egusphere-egu24-6299>

- Wang, J., Flierl, G. R., LaCasce, J. H., McClean, J. L., & Mahadevan, A. (2013). Reconstructing the ocean's interior from surface data. *Journal of Physical Oceanography*, *43*(8), 1611–1626. <https://doi.org/10.1175/JPO-D-12-0204.1>
- Watts, D. R., Tracey, K. L., Donohue, K. A., & Chereskin, T. K. (2016). Estimates of eddy heat flux crossing the Antarctic circumpolar current from observations in Drake Passage. *Journal of Physical Oceanography*, *46*(7), 2103–2122. <https://doi.org/10.1175/JPO-D-16-0029.1>
- Wolfe, C. L., Cessi, P., McClean, J. L., & Maltrud, M. E. (2008). Vertical heat transport in eddying ocean models. *Geophysical Research Letters*, *35*(23), L23605. <https://doi.org/10.1029/2008GL036138>
- Yu, X., Garabato, A. C. N., Martin, A. P., Buckingham, C. E., Brannigan, L., & Su, Z. (2019). An annual cycle of submesoscale vertical flow and restratification in the upper ocean. *Journal of Physical Oceanography*, *49*(6), 1439–1461. <https://doi.org/10.1175/JPO-D-18-0253.1>
- Zhang, Z., Liu, Y., Qiu, B., Luo, Y., Cai, W., Yuan, Q., et al. (2023). Submesoscale inverse energy cascade enhances Southern Ocean eddy heat transport. *Nature Communications*, *14*(1), 1335. <https://doi.org/10.1038/s41467-023-36991-2>